Genome Medicine

RESEARCH

Open Access

RNA polymerase I is essential for driving the formation of 3D genome in early embryonic development in mouse, but not in human

Changliang Hou[1†], Geng G. Tian[1,2*†], Shuanggang Hu[3,4†], Beili Chen[5†], Xiaoyong Li[1†], Bo Xu[1†], Yuedi Cao[1†], Wei Le[6], Rong Hu[7], Hao Chen[8], Yan Zhang[9], Qian Fang[1], Man Zhang[10], Zhaoxia Wang[10], Zhiguo Zhang[5], Jinfu Zhang[11], Zhaolian Wei[5], Guangxin Yao[3,4], Yefan Wang[12], Ping Yin[13], Ya Guo[12], Guoqing Tong[14*], Xiaoming Teng[15*], Yun Sun[3,4*], Yunxia Cao[5*] and Ji Wu[1,16*]

Abstract

Background Three-dimensional (3D) chromatin architecture undergoes dynamic reorganization during mammalian gametogenesis and early embryogenesis. While mouse studies have shown species-specific patterns as well as mechanisms underlying de novo organization, these remain poorly characterized in humans. Although RNA polymerases II and III have been shown to regulate chromatin structure, the potential role of RNA polymerase I (Pol I), which drives ribosomal RNA production, in shaping 3D genome organization during these developmental transitions has not been investigated.

Methods We employed a modified low-input in situ Hi-C approach to systematically compare 3D genome architecture dynamics from gametogenesis through early embryogenesis in human and mouse. Complementary Smart-seq2 for low-input transcriptomics, CUT&Tag for Pol I profiling, and Pol I functional inhibition assays were performed to elucidate the mechanisms governing chromatin organization.

Results Our study revealed an extensive reorganization of the 3D genome from human oogenesis to early embryogenesis, displaying significant differences with the mouse, including dramatically attenuated topologically associating domains (TADs) at germinal vesicle (GV) stage oocytes. The 3D genome reconstruction timing is a fundamental difference between species. In human, reconstruction initiates at the 4-cell stage embryo in human, while in mouse,

†Changliang Hou, Geng G. Tian, Shuanggang Hu, Beili Chen, Xiaoyong Li, Bo Xu and Yuedi Cao are equally contributed to this work.

*Correspondence:
Geng G. Tian
genetian@sjtu.edu.cn
Guoqing Tong
drivftongguoqing@xjtufh.edu.cn
Xiaoming Teng
tengxiaoming@51mch.com
Yun Sun
syun163@163.com
Yunxia Cao
caoyunxia6@126.com
Ji Wu
jiwu@sjtu.edu.cn
Full list of author information is available at the end of the article

it commences at the 2-cell stage embryo. We discovered that Pol I is crucial for establishing the chromatin structures during mouse embryogenesis, but not in human embryos. Intriguingly, the absence of Pol I transcription weakens TAD structure in mouse female germline stem cells, whereas it fortifies it in human counterparts.

Conclusions These observed interspecies distinctions in chromatin organization dynamics provide novel insights into the evolutionary divergence of chromatin architecture regulation during early mammalian development. Our findings provide mechanistic insights into species-specific chromatin organization during germ cell and embryonic development and have potential implications for fertility preservation and birth defect prevention.

Keywords Chromatin structure, Early embryonic development, Stem cell, Polymerase I

Background

In eukaryotic cells, genomic DNA exhibits a hierarchical three-dimensional (3D) organization, encompassing multiple structural levels from chromosome territories to chromatin compartments, topologically associating domains (TADs), and chromatin loops [1–4]. Through high-throughput chromosome conformation capture (Hi-C) technology, researchers have discovered that interphase chromosomes are spatially partitioned into two principal compartment types: A and B compartments, which represent a higher-order chromatin organization beyond TADs [5]. The A compartments are characterized by euchromatic regions featuring accessible chromatin structure and transcriptionally active genes, while B compartments comprise heterochromatic regions with condensed chromatin structure and transcriptionally silent genes [5]. The intricate chromatin architecture orchestrates various cellular process, including gene expression, DNA replication, and developmental processes [2, 4, 6, 7].

Several recent studies have reported changes in the chromatin structure during gametogenesis and embryonic development across various species. Our findings and others have revealed that compartments and the TAD structure weaken gradually during mouse oogenesis [8–10] and are not visible in mouse metaphase II (MII) oocytes [11, 12]. During mouse spermatogenesis, the TAD structure is weak in spermatogonia and pachytene spermatocytes, and enhanced in round spermatozoa [13]. Such chromatin reorganization has also been observed during rhesus monkey spermatogenesis [14]. Additionally, mouse sperm show a similar compartmentation pattern and TAD structure to those in somatic cells [11, 14–16]. Upon fertilization, the chromatin structure is relatively loose in mouse zygotes and becomes evident during embryonic development [11, 12]. In parallel, the chromatin structure is gradually established during drosophila zygotic genome activation (ZGA) [17]. Chen et al. showed that TAD structures and A/B compartments are absent in human 2-cell embryos, and weakly exist in human 8-cell embryos [18]. To date, the chromatin structure dynamics in human gametogenesis and embryos from the 4-cell to 8-cell stage and the divergence between humans and mice remain unclear.

Currently, there are a few studies that have investigated the mechanism of the chromatin structure in mammalian oogenesis and early embryos [8, 19]. Du et al. showed that depletion of polycomb repressive complex 1 reduces polycomb-associating domains in mouse oocytes, whereas depletion of EED (embryonic ectoderm development) destroys the polycomb-associating domain in mouse embryos [8]. Moreover, overexpression of lysine-specific demethylase 5B prevents formation of the lamina-associated domain structure in mouse embryos [19]. The roles of transcriptional and non-coding RNAs in chromatin structures have also been reported [20, 21]. During mammalian early embryonic development, nuclear transcription or ZGA is carried out by three distinct RNA polymerases, RNA polymerase (Pol) I–III, which mainly transcribe rRNA, mRNA, and tRNA, respectively [22]. In human embryos, the TAD structure disappears after inhibiting Pol II and III transcription, and CTCF plays an important role [18]. However, inhibition of Pol II and III transcription does not prevent establishment of TAD structures in mouse and drosophila embryos [11, 12, 17].

Pol I is usually composed of 14 subunits, of which the core subunits POLR1 A and POLR1B form the Pol I active center [23]. Its transcribed rRNA accounts for 60–70% of new RNA [24, 25]. With the exception of involvement in ribosome biogenesis, several studies have demonstrated that Pol I transcription is engaged in chromatin remodeling and maintenance of nucleolar integrity [26–29]. During the development of mouse GV oocytes from the non-surrounded nucleolus type to surrounded nucleolus type, Pol I transcription inactivates gradually, which is accompanied by chromatin compaction [30, 31]. After fertilization, Pol I transcription shows an obvious upward trend from the mouse 1-cell to 2-cell embryo [11, 12, 32, 33]. However, it remains unknown whether Pol I transcription contributes to regulation of chromatin structures during gametogenesis and early embryonic development in humans and mice.

In this study, we employed a modified low-input in situ Hi-C methodology to systematically characterize 3D genome architecture dynamics during human and mouse oogenesis and early embryogenesis, with focus on identifying species-specific chromatin reorganization patterns. Through an integrated multi-omics approach incorporating low-input transcriptomics, CUT&Tag, and functional genomic analyses, we elucidated the previously unrecognized role of RNA polymerase I in regulating chromatin architecture during these critical developmental transitions. Our work establishes the comprehensive cross-species comparison of Pol I-dependent chromatin regulation in mammalian germ cells and early embryos, providing fundamental insights with potential implications for understanding human reproductive biology and preventing developmental disorders.

Methods

Ethics statement

This study was approved by the institutional review boards of The Affiliated Ren Ji Hospital of Shanghai Jiao Tong University (2,019,122,701), Affiliated Tongji Hospital of Tongji University (2020-KYSB- 048), Shanghai First Maternity, and Infant Hospital (KS21280), The First Affiliated Hospital of Anhui Medical University (2020H026), and Shuguang Hospital Affiliated to Shanghai University of Traditional Chinese Medicine (2020–866 - 75–01). The study was conducted in accordance with the measures of the People's Republic of China on the administration of human-assisted reproductive technology, the ethical principles of human assisted reproductive technology, and the Helsinki declaration. Briefly, testicular biopsies were obtained from obstructive azoospermic patients who underwent microdissection at the Affiliated Tongji Hospital of Tongji University. Human sperm with normal fertility was collected from the Shanghai First Maternity and Infant Hospital. Human oocytes and early embryos were obtained from Shanghai Jiao Tong University Affiliated Ren Ji Hospital and the First Affiliated Hospital of Anhui Medical University. Volunteers were informed that their gametes and embryos would be used to study the chromatin structure and its regulation during human embryo development. All volunteers signed an informed consent document.

Animals

ICR/CD1 mice were purchased from SLAC Laboratory (Shanghai, China) and housed at the Laboratory Animal Center of Shanghai Jiao Tong University. The husbandry practices for the mice included maintaining them in an environment with automatically controlled temperature and humidity, under a 12-h light/12-h dark cycle, and providing them with ad libitum access to food and water. Euthanasia of the mice was performed using carbon dioxide inhalation followed by cervical dislocation. All animal experiments were conducted in accordance with the recommendations of the Guide for the Care and Use of Laboratory Animals and relevant Chinese laws and regulations, and were approved by the Institutional Animal Care and Use Committee (IACUC) of Shanghai Jiao Tong University (Spatiotemporal dynamics and regulatory mechanisms of gametogenesis and embryonic development in mammals, A2019118).

Human samples

Follicular aspirates (FAs) were obtained from a total of 213 consenting donors (aged 30–45 years) with tubal-factor infertility following written informed consent. After clinical oocyte retrieval, residual FAs from multiple patients were collected in sterile conical tubes and transported to the laboratory at ambient temperature within 2 h for processing. High-quality embryos were randomly selected for analysis, with selection constrained by limited cell availability. All specimens were collected and handled according to established clinical protocols.

Human gamete and early embryo collection

Human sperm was incubated in human tubal fluid medium for 30 min in a CO_2 incubator at 37 °C. After several washes with human tubal fluid medium, swim-up sperm were collected for experiments. Human oocytes were collected from volunteers who underwent assisted reproductive technology because of tubal factor infertility. GV and MII oocytes were identified using microscopy by the presence of a nucleus (GV oocytes) or first polar body (MII oocytes). The surrounding cumulus cells attached to the oocytes were removed using hyaluronidase. All oocytes were washed with PBS before experiments.

All human early embryos used in this study had normal development rates and morphology. For two pronuclei embryo samples, 4-cell and 8-cell embryos, and blastocysts were derived from ICSI rather than IVF to avoid potential contamination by cumulus cells and sperm. Fertilization was verified at 16–19 h after ICSI, and embryo cleavage was recorded every 24 h. Additionally, 8-cell embryos from zygotes with three pronuclei were collected, which exhibited high-quality morphology without developmental arrest. For consistency of sample collection, all donated oocytes and embryos were vitrified in liquid nitrogen for storage and sample pooling before thawing, and the zona pellucida was removed with acid Tyrode's solution prior to Hi-C. The numbers of oocytes and embryos used in this study are summarized in Supplementary Table S1.

Collection of mouse early embryos

All animal experiments followed procedures approved by the Institutional Animal Care and Use Committee of Shanghai Jiao Tong University (Number: A2016084). Six to eight-week-old ICR/CDl mice were housed in a specific pathogen-free (SPF) facility under controlled conditions (temperature: 22 ± 1 °C, humidity: 50 ± 10%; 12-h light/dark cycle) with ad libitum access to standard·chow and sterile water. Mouse embryos were collected from 6–8-week-old ICR/CD1 mice. Briefly, female mice were superovulated by an intraperitoneal injection of 10 IU pregnant mare serum gonadotrophin, followed by a human chorionic gonadotropin (hCG; 10 IU) injection 48 h later. Superovulated females were mated with ICR/CD1 males. For euthanasia, mice were subjected to·CO_2, inhalation followed by cervical dislocation, as per AVMA guidelines. Zygotes were collected from the oviducts of female mice at 20 h post-hCG injection and cultured in KSOM medium. Early 2-cell, late 2-cell, 4-cell, 8-cell, morula, and blastocyst stage embryos were harvested at 34 h, 47 h, 56 h, 68 h, 80 h, and 3.5 days post-hCG injection, respectively.

Culture of female germline stem cells

Human and mouse FGSCs were established and cultured in our laboratory as reported previously [34–37]. Briefly, dissected ovarian tissues were digested with collagenase IV and trypsin. The samples were further purified by magnetic beads coupled to anti-MVH antibody. The purified FGSCs were cultured on mitotically inactivated mouse STO cell feeders treated with 10 μg/ml mitomycin C (Sigma) at 37 °C with 5% CO_2. Cells were passaged every 3–4 days at a ratio of 1:4 and the medium was replaced every 2 days.

Reverse transcription-PCR (RT-PCR) and quantitative RT-PCR

Total RNA from cells was extracted with TRIzol reagent and reverse transcribed into cDNA. Single-embryo RT-PCR was performed as described previously [38]. Quantitative RT-PCR was performed with Power SYBR Green PCR Master Mix. Relative mRNA levels were calculated after normalization to GAPDH. Primers are listed in Additional File 3: Table S2.

Immunofluorescence staining

Cultured germline stem cells and embryos were fixed in a 4% paraformaldehyde solution in PBS at room temperature for 30 min. Then, cells were permeabilized with 0.5% Triton X- 100 for 30 min at room temperature. After wishing with PBS three times, the cells were blocked with goat serum at room temperature for 30 min, followed by overnight incubation at 4 °C with appropriate primary antibodies. After washing with PBS containing 0.05% Tween- 20, the cells were incubated with secondary antibodies for 45 min and then incubated with 4′,6-diamidino- 2-phenylindole at 37 °C for 10 min. Petri dishes were covered with antifade mounting medium and photographed.

Western blotting

Embryos were rinsed with PBS to remove debris and then lysed in SDS sample buffer for 5 min at 98 °C. Total proteins were separated on SDS-PAGE gels and transferred to PVDF membranes, followed by blocking in TBST containing 5% dry non-fat milk powder at room temperature. The membranes were incubated with primary antibodies overnight at 4 °C. Then, the membranes were washed three times with TBST and incubated with an appropriate HRP-linked secondary antibody for 1 h at 37 °C, followed by washing with TBST three times. Bound antibodies were detected by enhanced chemiluminescence.

In vitro transcription and preparation of mRNA for microinjection

To prepare EGFP mRNA for microinjection, the EGFP gene was amplified from a pcDNA3.1-EGFP plasmid with T7 promoter sequence primers and used as a template. The operations were carried out in accordance with the kit instructions (AM1745; Invitrogen). Synthesized mRNA was purified by lithium chloride precipitation and resuspended in nuclease-free water.

Knockdown of POLR1 A in mouse embryos

Sequences were pasted into the RNA fold online tool (http://rna.tbi.univie.ac.at/cgi-bin/RNAWebSuite/RNAfold.cgi). Minimum free energy was selected, and protospacers of 28 nucleotides (target sequences) with high accessibility (Lorenz et al., 2011) were chosen and chemically synthesized by TsingKe biological technology. CRISPR-LwaCas13a protein was purchased from Huicheng Biological Technology Co., Ltd. Cas13a protein (50 μg/μL), gRNAs (200 ng/μL), and EGFP mRNA were injected into 1-cell embryos. Each embryo was microinjected with approximately 5–10 pL. Microinjected embryos were washed with M2 medium and cultured in prewarmed KSOM medium covered with mineral oil (Sigma, M5904) at 37 °C with 5% CO_2. The ssRNA for crRNA spacer truncations sequences were as followed: 5′-GAUUUAGACUACCCCAAAAACGAAGGGGACUAAAACUUUAACACUUAACUUCUUGAGCUCUUCG- 3′ for POLR1 A- 2, and 5′-GAUUUAGACUACCCCAAAAACGAAGGGGACUAAAACACAGGUAAAUUGCAGCCCGAGGACAAGU- 3′ for POLR1 A- 1.

Transcription inhibition assay

α-Amanitin (0.1 mg/mL) or CX- 5461(0.1–3 mM) were added to culture medium at the indicated concentrations.

In situ Hi-C library generation using low cell numbers

In situ Hi-C following established published protocols with minor modifications for low cell numbers [9, 39, 40]. Briefly, the zona pellucida was removed using acidic Tyrode's solution (Sigma) before fixation in 1% formaldehyde (10 min, at room temperature). After glycine quenching, cells were pelleted (3000 *g*, 5 min, 4 °C) and lysed in ice-cold Hi-C lysis buffer (≥ 30 min). Chromatin was digested overnight with DpnII (NEB) at 37 °C following SDS/Triton X- 100 treatment. Restriction ends were filled with biotin- 14-dATP (Life Technologies) using DNA Polymerase I (NEB) at 24 °C for 4 h, followed by proximity ligation with T4 DNA ligase incubated at room temperature for 4 h with rotation and then transfer to 4 °C for 16 h with rotation. After proteinase K digestion (55 °C, 30 min), 10 µl DNA-Be-Down (B544732 -0001, Sangon Biotech) and 2.5 ×volumes of pure ethanol and 0.23 ×volumes of 3 M sodium acetate, pH 5.2, were added to the tube. The sample was mixed by inversion, incubated at −80 °C for 15 min, and then centrifuged at 13,000 rpm for 15 min at 2 °C. The supernatant was removed, and the pellet was washed twice with 75% ethanol and then dissolved 43 µl of 1× Tris buffer (10 mM Tris–HCl, pH 8). Then processed for end repair, A-tailing, and adaptor ligation (Vazyme kit ND607 -01). USER enzyme (NEB) treatment (37 °C, 15 min) opened adaptor loops before streptavidin bead capture (MyOne T1 Dynabeads, Life Technologies). Final libraries were amplified (15 cycles) using indexed primers (NEB E7335S) and VAHTS HiFi mix, then purified with AMPure XP beads (Beckman Coulter) for Illumina sequencing.

Hyperactive in situ ChIP

A hyperactive in situ ChIP assay was performed in accordance with the manufacturer's instructions (Vazyme, TD901 -01). Briefly, ConA-beads were washed once with binding buffer and incubated with zona pellucida-removed 2-cell embryos. Bead-bound cells were resuspended in antibody buffer containing a primary rabbit monoclonal anti-POLR1 antibody (24,799, Cell Signaling Technology) or negative control IgG (sc- 2025, Santa Cruz) for 2 h with slow rotation. The primary antibody was removed using a magnet stand. Then, bead-bound cells were incubated in Dig-wash buffer containing a secondary rabbit anti-mouse IgG H&L antibody (ab6709, abcam). Cells were incubated with Hyperactive pA-Tn5 Transposase adapter mix and then resuspended in tagmentation buffer. DNA was purified by phenol–chloroform-isoamyl alcohol extraction and ethanol precipitation, and treated with RNase A. Then, library amplification and PCR product purification were performed.

Detection of RNA synthesis

Mouse embryos were incubated with 50 mM EU for 5 h, fixed in 100% methanol for 20 min at −20 °C, and stained using a Cell-Light EU RNA labeling kit (Ribobio, Guangzhou, China) for nascent RNA analysis. Imaging of embryos was performed under a Zeiss LSM710 confocal microscope.

RNA fluorescence in situ hybridization (FISH)

Embryo fixation was performed as described previously (Lin et al., 2014). Embryos were fixed using methanol, permeabilized using 70% ethanol. In accordance with the manufacturer's instructions (GenePharma, Beijing, China), hybridization was carried out at 37 °C overnight with mixed two independent probes (Kent et al., 2009). Probe sequences are 5′-CCACAGTTATCCAAGTAG GAGAGGAGCGAG- 3′ for 18S rRNA probe and 5′-ACAATGACCACTGCTAGCCTCTTTCCCTT- 3′ for ETS probe.

RNA-seq library preparation and sequencing

RNA-sequencing (RNA-seq) was conducted by the Smart-seq method [41, 42]. Briefly, lysed mouse embryo samples underwent reverse transcription with oligo-dT primers specifically annealing to the polyadenylated (poly-A) tails of mRNA molecules, ensuring selective capture of mRNA during complementary DNA (cDNA) synthesis. The resulting cDNA was pre-amplified using KAPA HiFi HotStart polymerase followed by purification. After purification, amplified cDNA was used for library construction. A single-strand circularization process was subsequently performed to generate a single-stranded circular DNA library harboring >200 copies of DNA nanoballs, which was sequenced on the BGISEQ500 platform.

CUT&Tag assay

CUT&Tag was performed with Hyperactive In-Site ChIP Library Prep Kit (Vazyme Biotech, #TD901) with modifications from established protocols [43]. Briefly, embryos were first transferred from KSOM culture medium to acidic Tyrode's solution droplets under a stereomicroscope to remove the zona pellucida, followed by a wash buffer to ensure clean starting material. The zona-free embryos were then carefully collected into a 1.5-mL EP tube containing 100 µL wash buffer. For cell immobilization, concanavalin A-coated magnetic beads were

prepared by washing twice with 100 μL binding buffer before being added to the embryo-containing tube. The embryo-bead mixture was gently rotated at room temperature for 10 min to facilitate binding. After removing the supernatant, the bead-bound embryos were resuspended in 50 μL antibody buffer containing rabbit anti-POLR1 A primary antibody (CST, #24,799, 1:50). Antibody incubation was performed either at room temperature for 2 h. After washing twice with dig-wash buffer, secondary antibody was added and incubated at room temperature for 45 min. Following two washes with dig-wash buffer, 100 μL of dig- 300 buffer was supplemented with 0.04 μL pG-Tn5 transposase. The samples were incubated at room temperature for 1 h, then subjected to two additional dig-wash buffer washes. Subsequently, 300 μL of tagmentation buffer was added and the reaction mixture was incubated at 37 °C for 1 h. The reaction was stopped by adding 10 μL 0.5 M EDTA, 3 μL 10% SDS, and 2.5 μL 20 mg/mL Proteinase K, with incubation at 55 °C for 1 h. Following phenol–chloroform extraction and ethanol precipitation, the DNA libraries were amplified by PCR (16 cycles). Finally, all libraries were sequenced using Illumina HiSeq with 150-bp paired-end reads.

Cell viability assay

A cell viability assay was conducted using a CCK- 8 kit. FGSCs were seeded in 96-well plates and treated with drugs for the indicated time. Then, the optical density value at 450 nm was measured in accordance with the manufacturer's protocol.

Cell proliferation assay

The cell proliferation rate was measured using an EdU Cell Proliferation Assay Kit (Ribobio, Guangzhou, China). In brief, FGSCs were seeded in 48-well plates and treated with drugs for a certain time. FGSCs were incubated with 50 μM EdU for 2 h, followed by fixation and permeabilization. Nuclei were labeled with 4′,6-diamidino- 2-phenylindole for 6 min and visualized under a fluorescence microscope.

Cell cycle analysis

Cell cycle analysis was performed as described previously [37]. In brief, cells were washed with pre-cooled phosphate-buffered saline (PBS) and digested with trypsin. Then, cells were fixed with 70% ice-cold ethanol overnight at 4 °C. After washing twice with ice-cold PBS, the cells were stained with propidium iodide solution (10 μg/ml) containing RNAase A for 30 min. Subsequently, the cell cycle distribution was analyzed using a CytoFLEX S flow cytometer. Results were analyzed using FlowJo software.

Data analysis

Hi-C data processing

Hi-C data were processed as described previously [9, 44]. In brief, adaptor sequences in raw reads were trimmed with Cutadapt (version 1.0), and low-quality paired-end reads were filtered with BBmap (version 38.16). Sequence reads were separately mapped to the reference genome using Bowtie2 software. After filtering out self-ligated reads and uncut reads, ICE normalization was performed using the ICE algorithm implementation. Subsequently, the HiTC R package was used to analyze HiC interactions contact matrices.

Reproducibility of Hi-C data

The reproducibility score was measured by the HiCRep method [45]. In brief, we calculated the number of interactions at each point within the maximum 2 Mb and then counted the possible interactions between two replicates.

Contact probability as a function of the genomic distance p(s)

Contact probability versus genomic distance [P(s)] curves were constructed as described previously. We counted the number of Hi-C contacts and calculated the number of possible Hi-C contacts at a certain distance across the genome. Contact probability P(s) was derived by dividing the contact number by potential contacts. P(s) was then normalized by setting the value of P(s) at various distances.

Analysis of the chromatin compartments status (A/B compartment)

Genomic compartments were calculated using principal component analysis on contact maps at a 500 kb resolution. We used HiTC package in R to calculate the A/B compartment status. Normalized matrices at 500 kb resolution were calculated the first eigenvectors with the pca.hic function with default parameters. Positive eigenvector values were assigned to compartment A and negative eigenvector values were assigned to compartment B. The compartment strength was calculated as described previously. A saddle plot was constructed by the formula log[AA + BB/(AB + BA)], where AA, AB, BA, and BB represent the four corners of the iteratively corrected saddle plot matrix.

TADs, TAD boundaries, and TAD signal calculation

TADs and TAD boundaries/insulators were identified by previously described methods [5, 46]. Briefly, a sliding window at 500 kb on 40 kb-binned contact maps was used to analyze the insulation score. The signal within the sliding window was assigned to the corresponding bin across the entire genome. The insulation score was

normalized by calculating the log2 ratio of individual scores and the mean of genome-wide averaged insulation scores. TAD boundaries/insulators were identified by calling the local minima along the normalized insulation score.

Identification of chromatin loops

Chromatin loops were identified using the JUICER package. Briefly, filtered read-pairs from HiC data were converted into.hic format files and inputted into HiCCUPS. The parameters used in this study were Xmx256 g, -m 1024, and –ignore_sparsity. Chromatin loops with $P < 0.001$ were merged together as the final chromatin loop.

RNA-seq analysis

All lean reads were aligned to the reference genome (mm9 version) by Hisat2 software with default parameters. FPKM values (fragments per kilobase per million mapped reads) were then quantified per sample with Cufflinks, which normalizes raw counts by transcript length (per kilobase) and sequencing depth (per million scaling factor) using a protein-coding gene GTF annotation file.

Gene ontology analysis

Gene Ontology (GO) enrichment analysis was performed using the clusterProfiler R package [47], focusing specifically on biological process terms. Enrichment significance was determined using modified Fisher's exact test (FDR < 0.05), implemented similarly to the DAVID functional annotation tool.

CUT&Tag data analysis

Sequencing reads were quality-trimmed and aligned to the reference genome using HISAT2 (–no-spliced-alignment –no-temp-splicesite). Picard software was used to remove the PCR duplicates with MarkDuplicates function. Peak calling was performed using MACS2 (q-value < 0.05) followed by genomic annotation with HOMER [48]. Differential binding analysis was conducted using DiffBind software with default parameters [49]. Data visualization was achieved through heatmaps generated by deepTools (v3.5.1) [50]. For functional annotation, we performed (1) motif enrichment analysis using HOMER (findMotifsGenome.pl) and (2) genomic region enrichment analysis through GREAT (v4.0.4) [51].

Quantification and statistical analysis

Statistical analysis was conducted by R and GraphPad Prism. Significant difference between two samples was calculated by one-way ANOVA or Student's test. $P < 0.05$ was considered as statistically significant "*", $P < 0.01$ was indicated by "**" and $P < 0.001$ was indicated by "***".

Results

Recombination landscape of the chromatin structure during human FGSC development

To determine the 3D chromatin structure during human gametogenesis and early embryonic development, we collected female germline stem cells (FGSCs), hGV oocytes, hMII oocytes, sperm, and embryos at 4-cell, 8-cell, and blastocyst stages (Fig. 1A). All clinical tissues and embryos were collected after obtaining written informed consent from the donor. hFGSCs were isolated in our laboratory [34]. The collected cells were confirmed by RT-PCR and immunofluorescence staining (Additional file 1: Fig. S1 A–D). After filtering artificial reads and normalization, we obtained 10.8 billion reads by the low-input genome-wide chromosome conformation capture (Hi-C) method (Additional file 2: Table S1) [5, 11, 12]. The Hi-C data were highly reproducible between replicates, and Hi-C data from blastocysts were consistent with published data (Additional file 1: Fig. S2).

We examined the dynamics of chromatin architecture during hFGSC development using multiple analytical approaches. Chromatin interactions were visualized through heatmaps and quantified using directional indices (DIs), which measure the bias between upstream and downstream chromatin interactions for each genomic bin. TAD boundaries are characterized by sharp transitions from upstream to downstream interaction preferences, with higher DI values indicating more distinct boundary formation. Interaction maps of hFGSC phases

(See figure on next page.)

Fig. 1 Dynamic TADs and chromatin compartmentalization during human FGSC development. **A** Morphology of human germ cells and early embryos. Scale bar, 50 μm or 10 μm (Sperm). **B** Normalized Hi-C interaction frequencies displayed as a heatmap (top) and TAD signals (bottom) during hFGSC development at chromosome 10. **C** Average insulation scores (IS) of various stages at TAD and nearby regions. IS measures the frequency of chromatin interactions across a given genomic position, with local minima indicating potential TAD boundaries where cross-boundary interactions are depleted. A lower insulation score suggests stronger boundary activity. **D** Percentage of switched A/B compartments occupied in the genome during hFGSC development. **E** Saddle plot showing the compartment strength of (A+A) and (B+B) during hFGSC development. **F** Violin plot showing the change in compartment strength during hFGSC development (Wilcox test, ***$p<0.001$, ns: $p>0.05$). **G** Average contact probability across the genome was decreased as a function of genomic distance between humans and mice during FGSC development. **H** Percentage of inter-chromosomal and intra-chromosomal contacts between humans and mice during FGSC development. **I** Compartment strength between humans and mice during FGSC development ($P<0.05$, calculated by the Wilcoxon test)

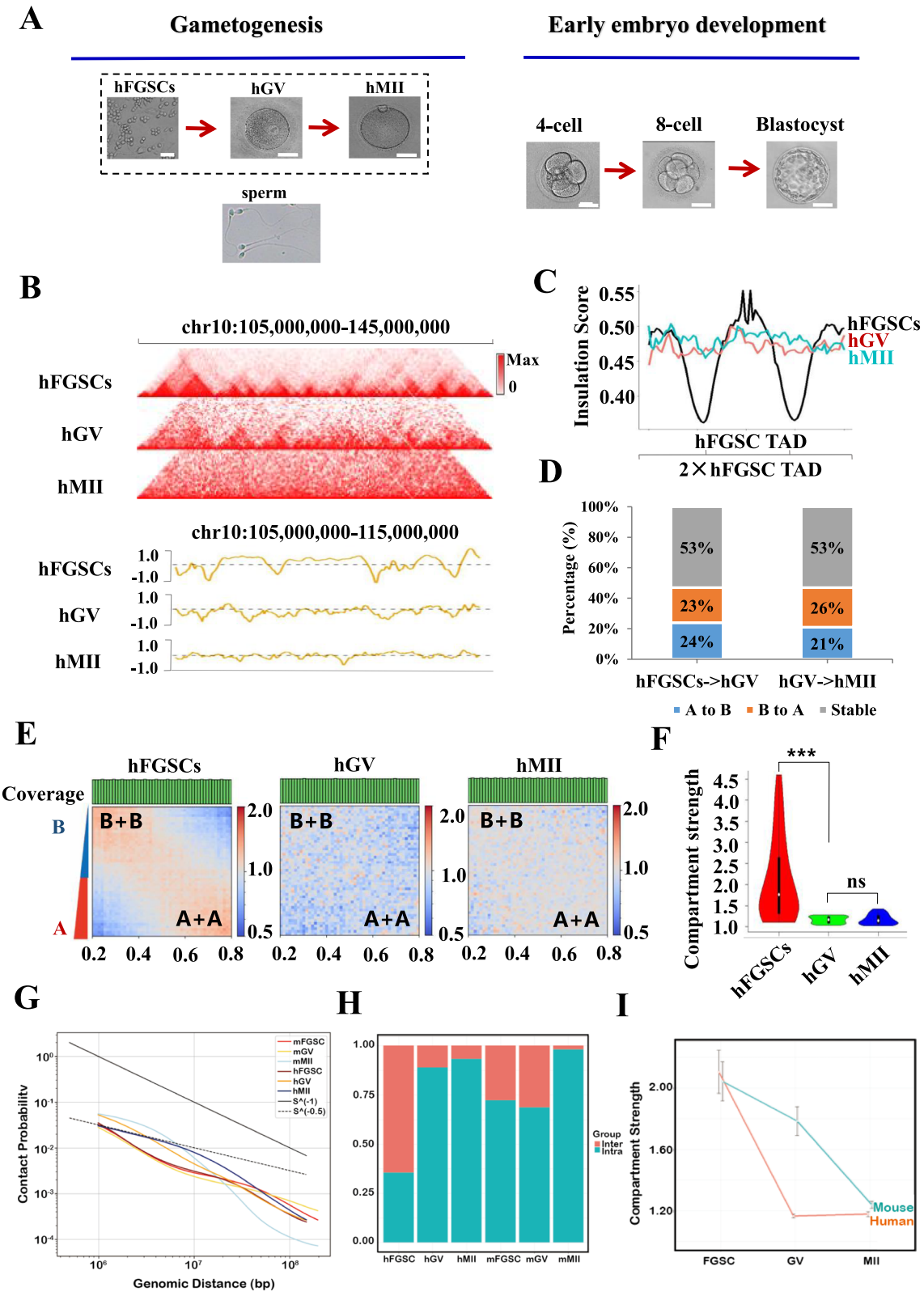

Fig. 1 (See legend on previous page.)

displayed obvious triangular patterns of regional enrichment, while they were weakened in hGV oocytes. No triangular patterns are observed in hMII oocytes (Fig. 1B), which was consistent with findings in mice [11, 12]. After calculating the average intrachromosomal contact probability, hGV oocytes had a relatively higher contact probability between 1×10^5 bp and 1×10^6 bp, but lower contact probability outside this distance range. However, hMII oocytes showed a relatively higher contact probability between 1×10^7 bp and 1×10^8 bp, and hFGSCs had an upward tread beyond 1×10^8 bp (Additional file 1: Fig. S3 A). Additionally, the *P(s)* curve of hMII oocytes between 1×10^5 bp and 1×10^7 bp was very similar to the previously reported *P(s)* 0.5 for mitotic cells [52]. We then analyzed the contact probability dependence on the genomic distance. Unlike the other stages, the hGV oocyte interaction was not only enriched near 1×10^8 bp, but also more enriched in the medium distance from 1×10^5 bp to 1×10^6 bp (Additional file 1: Fig. S3B). These results indicate that the chromatin conformation undergoes global reorganization during hFGSC development.

We then investigated TAD organization across different developmental stages of hFGSCs. Our analysis revealed robust TAD structures in hFGSCs that progressively diminished, ultimately becoming undetectable in hMII oocytes (Fig. 1B). This observation was corroborated by directional index (DI) analysis, which showed a significant reduction in DI values during the transition from hFGSCs to hGV oocytes (Additional file 1: Fig. S3 C). The insulation score (IS), which quantifies the frequency of chromatin interactions across specific genomic positions, further supported these findings. Local minima in the IS profile indicate potential TAD boundaries where cross-boundary interactions are depleted, with lower scores reflecting stronger boundary activity. Notably, hFGSCs exhibited markedly higher insulation scores compared to both hGV and hMII stages (Fig. 1C), indicating that TAD boundaries are most pronounced in hFGSCs and progressively weaken during oocyte development. In parallel with these structural changes, we observed extensive chromatin reorganization, whereby 50% of genomic regions demonstrated compartment A/B switching (Fig. 1D). This was accompanied by a systematic redistribution of chromatin compartments during hFGSC development, marked by the gradual enrichment of compartment A domains and a corresponding decrease in compartment B regions (Fig. 1E, Additional file 1: Fig. S3D, E). The compartment strengths in hFGSCs were relatively strong and significantly decreased in hGV and hMII oocytes (Fig. 1F). Analysis of genes within compartment-switching regions revealed stage-specific functional transitions, progressing from immune response and epithelial pathways (FGSC-to-GV) to ion homeostasis and JAK-STAT signaling (GV-to-MII) (Additional file 1: Fig. S3 F). These findings demonstrate a dramatic reorganization of higher-order chromatin architecture during oocyte maturation, ultimately leading to the dissolution of TADs in hMII oocytes.

To elucidate species-specific features of chromatin organization during FGSC development, we performed comparative analyses between human and mouse FGSC development. While both species undergo substantial chromatin remodeling, their specific patterns of reorganization differ significantly. Analysis of distance-dependent interaction frequencies revealed that both human and mouse MII oocytes exhibited similar power law exponents approaching 0.5 (Fig. 1G). However, the contact frequency dynamics differed markedly between species during FGSC development. Most notably, we observed substantial variation in contact probability patterns between hFGSCs and hGV stages, whereas mFGSCs and mGV stages maintained relatively consistent patterns (Additional file 1: Fig. S4 A). Human FGSCs exhibited a distinctive chromosomal interaction profile, marked by a lower frequency of intra-chromosomal contacts and increased inter-chromosomal interactions compared to mouse (Fig. 1H). This species-specific difference diminished in later stages, as both human and mouse oocytes showed a progressive decline in interaction frequency during the GV-to-MII transition. Additionally, chromosomal contact probabilities maintained a length-dependent relationship during the GV-to-MII transition in both species (Additional file 1: Fig. S4B). The dynamics of A/B compartmentalization also revealed species-specific patterns. In humans, A/B compartment segregation decreased dramatically during the hFGSC to hGV transition but remained stable between hGV and hMII stages. In contrast, mouse cells maintained stable A/B compartmentalization between mFGSC and mGV stages, with significant reduction occurring during the mGV to mMII transition (Fig. 1I). Both species exhibited similar temporal patterns in A/B compartment ratios for autosomes, characterized by an initial increase followed by a decrease. The X chromosome showed particularly interesting species-specific features: hMII oocytes maintained a higher proportion of A compartment regions compared to autosomes, while mMII oocytes displayed the opposite pattern (Additional file 1: Fig. S4 C). TAD organization showed progressive weakening during FGSC development in both species, as evidenced by declining relative TAD strength measurements (Additional file 1: Fig. S4D). These comprehensive analyses reveal both conserved features and species-specific differences in chromatin architecture dynamics during mammalian FGSC development.

TAD structures re-establish from the human 4-cell to 8-cell embryo

To investigate the dynamics of chromatin architecture during early human embryogenesis, we performed Hi-C analysis at 40 kb resolution across developmental stages from 4-cell embryos to blastocysts. Interaction heatmaps revealed systematic remodeling of chromatin spatial organization throughout early development (Fig. 2A, Additional file 1: Fig. S5 A). Notably, we observed weak but detectable TAD structures in 4-cell embryos, which progressively strengthened through the 8-cell stage, followed by a marked enhancement in blastocysts. This developmental progression of TAD establishment was further validated by quantitative metrics. Both the directional index (DI) values and TAD signals showed consistent increases from 4-cell embryos to blastocysts, with genome-wide analysis confirming this pattern (Fig. 2B, Additional file 1: Fig. S5B). Analysis of global interaction patterns revealed stage-specific characteristics. Contact probability curves demonstrated similar patterns among embryonic stages and sperm, while displaying distinct features from oocytes (Fig. 2C). Further examination of interaction distances showed that the ratio of long-range (> 2 Mb) to short-range (≤ 2 Mb) contacts peaked in sperm, reached its nadir in 8-cell embryos, and increased again in blastocysts (Fig. 2D), suggesting dynamic regulation of chromatin interactions during development. Compartment analysis revealed another layer of chromatin organization dynamics. The characteristic checkerboard pattern of A/B compartments was barely detectable in 4-cell and 8-cell embryos but emerged prominently in blastocysts, with compartment strength measurements supporting this observation (Fig. 2E, Additional file 1: Fig. S5 C). Principal component analysis provided additional evidence for this developmental transition, showing distinct bimodal PC1 value distribution exclusively in blastocysts, while earlier stages exhibited poor compartment segregation (Fig. 2F). Collectively, these findings demonstrate that higher-order chromatin organization emerges in a hierarchical manner during early human embryogenesis, with initial establishment of TADs at the 4-cell stage followed by progressive maturation through blastocyst formation. This sequential organization suggests a programmed establishment of chromatin architecture that may be essential for proper embryonic development.

Species-specific dynamics in higher-order chromatin organization during early embryonic development

To further investigate whether the higher-order chromatin organization varied between human and mouse embryos, we analyzed and compared published data of human and mouse embryos during mammalian early embryonic development with our data [39]. By counting whole genome contacts at various resolution, the proportion of cis-short interactions in 4-cell and 8-cell embryos was much higher than that in Blastocyte, which was similar in mice (Additional file 1: Fig. S6 A). The ratio of long-distance contacts (> 2 Mb) versus short-distance contacts (≤ 2 Mb) was also significantly different between 8-cell embryos and the ICM, and no significant difference was found between 4-cell and 8-cell embryos in humans and mice (Additional file 1: Fig. S6B). Next, we found that the proportion of intra-chromosomal contacts was higher than inter-chromosomal contacts in humans and mice (Additional file 1: Fig. S6 C). Interestingly, the human ICM had the highest inter-chromosomal contacts during early embryonic development, while the stage with the highest inter-chromosomal contacts was 2-cell embryos in mice (Additional file 1: Fig. S6 C). These findings indicated that the formation of higher-order chromatin structures follows a similar trajectory during early embryonic development in both humans and mice, yet the establishment processes exhibit species-specific differences. To gain deeper insights into the distinct processes of the chromatin architecture during early embryonic development, we compared compartments and TADs between humans and mice. While the compartment strength was strongest in the ICM during early embryonic development in both humans and mice, the dynamics of this process differed between the two species (Additional file 1: Fig. S6D). Specifically, in human embryos, the strength increased gradually from the 4-cell stage to the ICM, whereas in mouse embryos, it underwent a dramatic increase from the 2-cell to 8-cell stage, followed by

(See figure on next page.)

Fig. 2 Dynamic TADs and chromatin compartmentalization during early embryonic development. **A** Top: Heatmap showing the normalized Hi-C interaction frequency. Bottom: Barplot showing the directional index (DI) at various developmental stages. **B** Relative variation degree of TAD signals in human embryo. **C** Average contact probability across the genome decreases as a function of genomic distance during human early embryonic development. **D** The total interaction ratio between genome distance >2 Mb and ≤2 Mb during human early embryonic development (Wilcox test, ns: $p>0.05$, ***$p<0.001$).**E** Saddle plot showing the compartment strength of (A+A) and (B+B) during human early embryonic development. **F** Top: Pearson correlation heatmap of chromosome 2 in human early embryos at a 500 kb resolution during human early embryonic development. Bottom: Density plots of eigenvector values considering autosomes during human early embryonic development

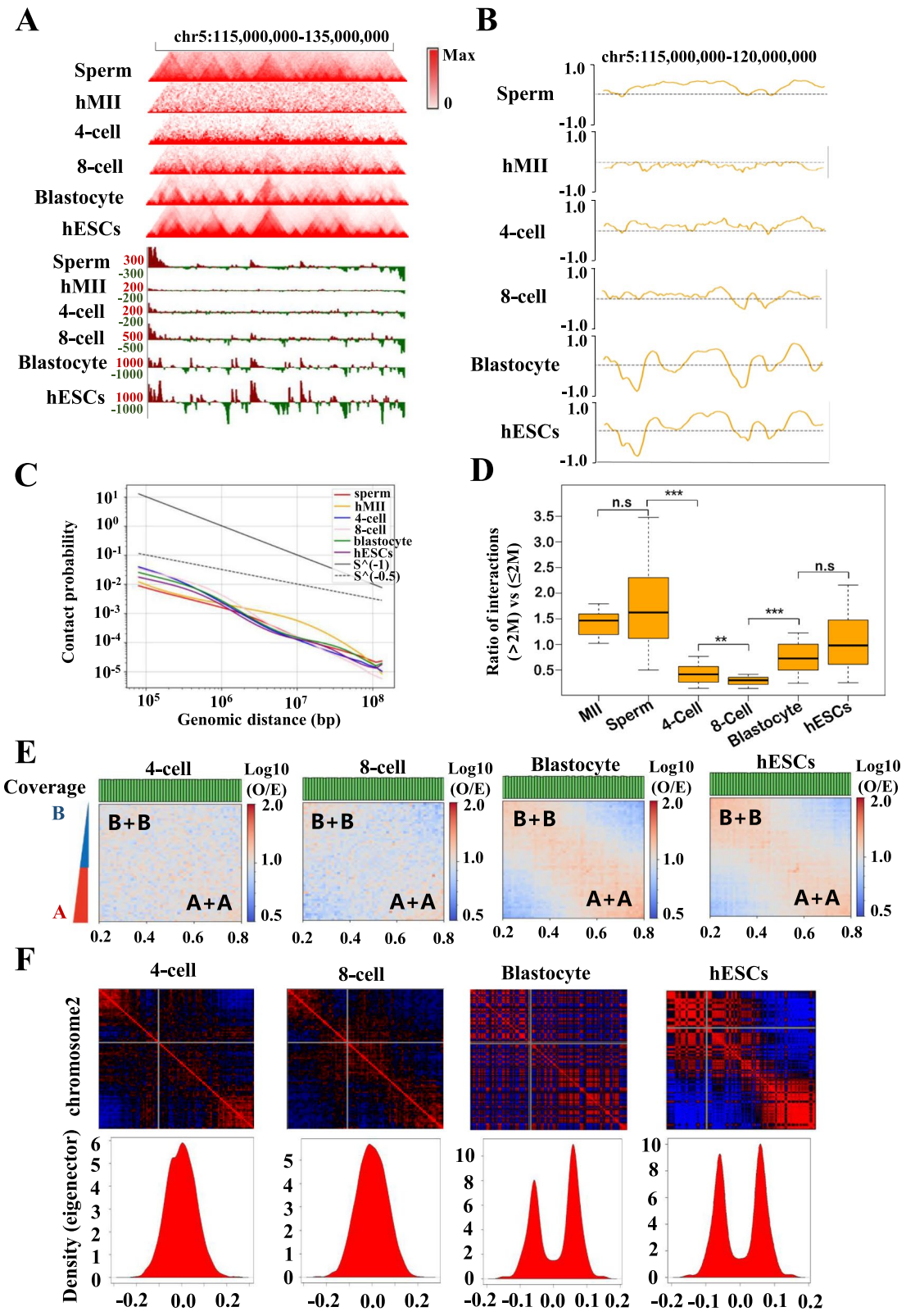

Fig. 2 (See legend on previous page.)

relatively little change from the 8-cell stage to the ICM (Additional file 1: Fig. S6D). Moreover, TAD insulation scores remained consistent between 4-cell and 8-cell stages in humans, whereas markedly rising in the ICM stage (Additional file 1: Fig. S6E). This suggests that TAD organization becomes more pronounced and refined during the ICM stage in humans. Conversely, such well-organized TADs are achieved by the 8-cell stage in mice [12, 39]. Additionally, the relative TAD strength increased gradually during early embryonic development in humans (Additional file 1: Fig. S6 F) and mice [12, 39]. These results suggested that different timing of TAD organization between human and mouse early embryos, the underlying molecular mechanisms may be simply activated at different developmental stages.

We next investigated the relationship between chromatin organization and zygotic genome activation (ZGA) during early embryonic development, we examined the temporal dynamics of transcriptional activation across species. While previous studies have demonstrated that topologically associating domain (TAD) establishment is ZGA-dependent in humans but ZGA-independent in mouse and drosophila embryos, these conclusions were primarily based on α-amanitin inhibition experiments, which specifically target RNA Polymerase II-mediated transcription while not addressing RNA Polymerase I activity [12, 17, 39]. To address this issue, we reanalyzed available bulk and single-cell RNA-seq datasets [53, 54]. The result revealed distinct species-specific patterns that mouse embryos exhibited a pronounced increase in RNA Polymerase I-associated transcripts during the early-to-late 2-cell transition, whereas human embryos showed elevated RNA Polymerase II-associated transcription during the 4-cell to 8-cell transition (Additional file 1: Fig. S6G). The temporal correlation between polymerase expression dynamics and species-specific chromatin organization timing motivated our subsequent investigation into the functional significance of RNA Polymerase I during early mammalian development.

RNA polymerase I is essential for TAD formation in mouse but not human early embryos

To elucidate the role of Pol I in the chromatin architecture establishment during mouse embryonic development, we performed immunofluorescence analysis to examine the spatiotemporal distribution of POLR1 A, the catalytic subunit of RNA Polymerase I. The result revealed that POLR1 A exhibited diffuse nuclear distribution in early 2-cell embryos, followed by granular aggregation in late 2-cell embryos, and ultimately showed predominant perinucleolar accumulation by the 4-cell stage, suggesting the distinct stage-specific localization patterns of Pol I (Fig. 3A). By permeating mouse zygotes with Carnot fixative, we also found POLR1 A in both the nuclear matrix and nucleolus (Fig. 3B), which was consistent with Pol I transcription in mouse zygote [55]. Moreover, we confirmed this finding by RNA-FISH with 18 s probes (Fig. 3C). Next, CRISPR/Cas13a + crRNA targeting POLR1 A was microinjected into mouse zygotes to explore the role of Pol I transcription (Additional file 1: Fig. S7 A). Knockdown efficiency of POLR1 A was verified by RT-PCR and western blotting (Additional file 1: Fig. S7B-E). Embryos with POLR1 A knockdown were blocked at the 2-cell stage, whereas the control group developed to the blastocyst stage (Additional file 1: Fig. S7 F). These data indicate that Pol I played a critical role in mouse early embryonic development.

To conform this finding, we treated zygotes (1-cell embryos) with CX- 5461, a specific inhibitor of Pol I. Consistently, mouse embryos were blocked in the 2-cell stage under treatment with 1.5 μM CX- 5461, and the rRNA transcription level was decreased significantly (Fig. 3D, E, Additional file 1: Fig. S7G). EU staining also showed that the fluorescence intensity was decreased after CX- 5461 treatment (Fig. 3F, Additional file 1: Fig. S7H). Simultaneously, inhibition of Pol I transcription reduced binding of POLR1 A at the rDNA site (Fig. S7I). These results suggest significant inhibition of Pol I transcription under CX- 5461 treatment. As expected, CX- 5461 treatment did not significantly disturb the expression levels of housekeeping genes and ZGA genes

(See figure on next page.)

Fig. 3 Pol I I plays a critical role in mouse early embryonic development. **A** Immunofluorescence of POLR1A in early mouse embryos fixed with paraformaldehyde. It is stained by the nucleolar marker B23 (Npm1, green), POLR1A (orange), and DAPI (blue). Scale bar, 50 μm. **B** Immunofluorescence of POLR1A in mouse zygotic embryos fixed with Carnoy's fixative. It is stained by the nucleolar marker B23 (Npm1, green), POLR1A (orange), and DAPI (blue). Scale bar, 50 μm. **C** RNA-FISH detection of Pol I transcription in mouse zygotic embryos. It is stained by pre-rRNA (red) and DAPI (blue). Scale bar, 50 μm. **D**Inhibition of Pol I transcription affected mouse embryonic development. Scale bar, 50 μm. **E** qRT-PCR was used to measure the rRNA transcription after CX-5461 treatment (Students' *t* test, ns: $p>0.05$, ***$p<0.001$). **F** EU detection of RNA transcription in mouse zygotic embryos. Scale bar, 50 μm. **G** Expression of ZGA genes and house-keeping genes in different condition of treatment. **H** Clustering analysis of differential gene expression patterns between control and CX-5461 inhibitor treatment. **I** GO enrichment analysis of different expressed genes after CX-5461 treatment for 45 h

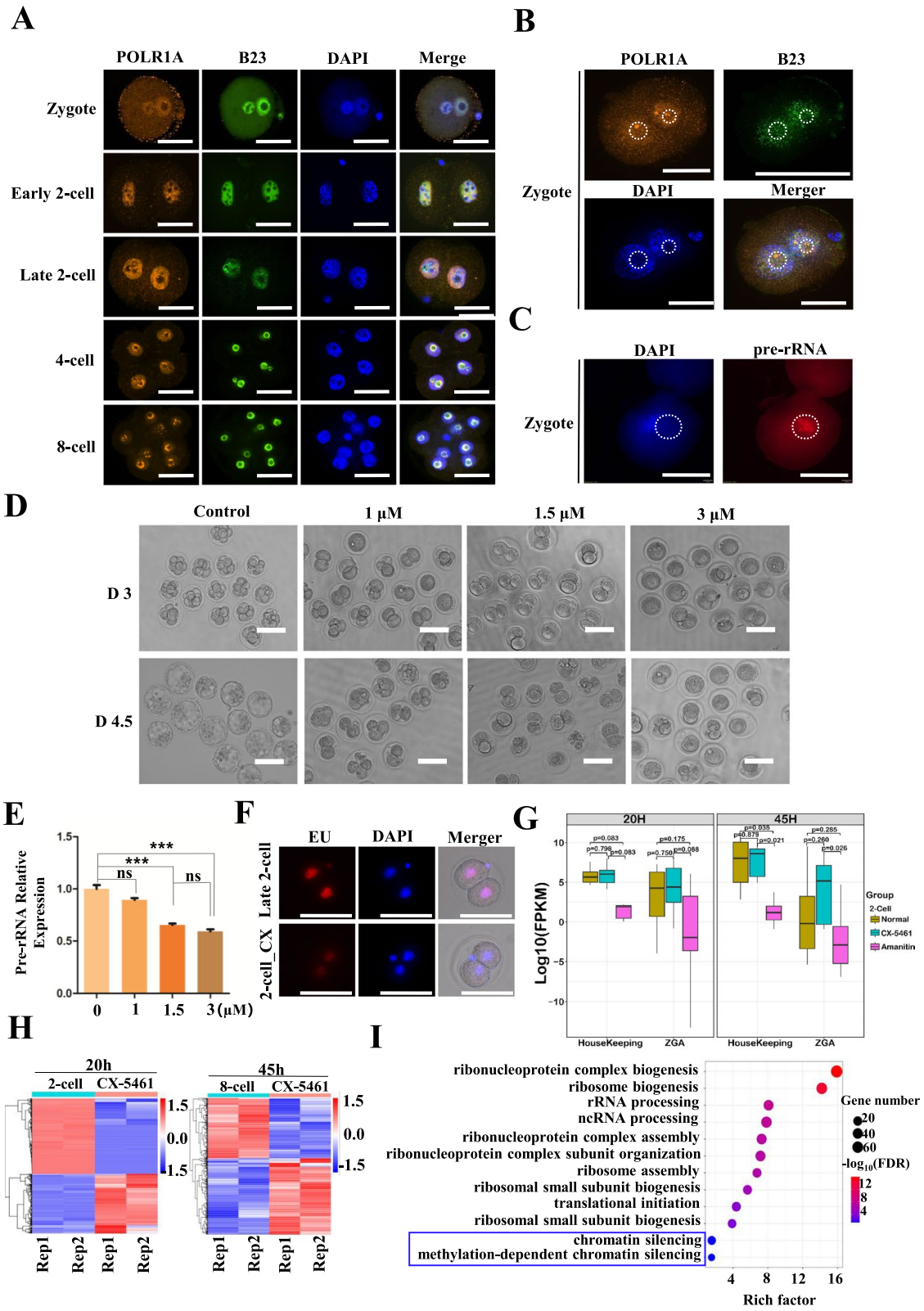

Fig. 3 (See legend on previous page.)

(Fig. 3G, Additional file 4: Table S3), although the overall mRNA transcription levels were initially reduced and then restored by CX- 5461 treatment. This pattern contrasts with the sustained low mRNA levels observed after inhibition of RNA polymerase II (Pol II) transcription (Additional file 1: Fig. S7 J). Our data demonstrate that CX- 5461 treatment specifically inhibits rRNA transcription without disturbing the expression levels of housekeeping genes and ZGA genes. Additionally, *Zscan4 d* and *GM12794*, which are zygotic genome activation (ZGA)-related genes, were normally transcribed after Pol I transcriptional inhibition. However, treatment with α-amanitin, a specific inhibitor of Pol II, suppressed transcription of both of them (Fig. S7 K). The effects of α-amanitin were profound, causing developmental arrest at the 2-cell stage and preventing further cell division. This developmental block underscores the critical role of Pol II-mediated transcription in early embryonic cell cycle progression and zygotic genome activation. Hierarchical clustering analysis of differentially expressed genes (DEGs) revealed distinct transcriptional profiles between control and CX- 5461-treated groups, as shown in the expression heatmap (Fig. 3H). Further analysis showed that gene ontology (GO) categories were enriched in ribonucleoprotein assembly, ribosome biogenesis, and rRNA processing (Fig. 3I), which was consistent with previously reported findings [56]. Among these, we identified 13 key epigenetic regulators that were significantly enriched in chromatin silencing and methylation-dependent chromatin silencing pathways, including HDAC1, POU5 F1, and notably TRIM28—a well-characterized heterochromatin marker. This enrichment pattern, particularly the presence of chromatin-modifying factors, suggests that inhibition of Pol I transcription leads to substantial changes in chromatin conformation, potentially through modulation of heterochromatin organization (Fig. 3I).

Next, we collected embryos treated with CX- 5461 for 45 h to examine the effect of Pol I transcription on the chromatin structure. Combined with Hi-C data from a public database [11], the interaction pattern was relatively vague in CX- 5461-treated 2-cell embryos. In contrast, α-amanitin-treated 2-cell embryos exhibited distinct interaction patterns resembling those of the 8-cell stage (Fig. 4A). TAD boundaries were less pronounced in CX-5461-treated 2-cell embryos but were well-defined in α-amanitin-treated 2-cell embryos (Additional file 1: Fig. S8 A). Further genome-wide TAD normalization analysis revealed that CX- 5461 treatment resulted in weakened TAD strength compared to the α-amanitin-treated group, showing characteristics more similar to the 2-cell stage (Fig. 4B). These observations were corroborated by the reduced insulation score following Pol I inhibition (Additional file 1: Fig. S8B), suggesting that Pol I might influence early embryonic development by modulating TAD strength. Additionally, we calculated the average intrachromosomal contact probability in normal 2-cell embryos, α-amanitin-treated, and CX- 5461-treated groups (Fig. 4C). While the overall differences were modest, substantial variations in chromatin long-range interactions emerged at genomic distances exceeding 10^7 bp. Comparison of short-range versus long-range interaction frequencies revealed that the α-amanitin-treated group exhibited a higher proportion of long-range interactions, whereas CX- 5461 treatment significantly reduced the frequency of long-range interactions, although this proportion remained elevated compared to the 2-cell stage (Fig. 4D). Collectively, these results indicate that inhibition of Pol I transcription prevents establishment of the TAD formation during mouse early embryonic development (Fig 5).

To investigate whether Pol I did function in early embryonic development in human, we treated human embryos with CX- 5461 were blocked at the 8-cell stage, while the control group developed to the blastocyst stage (Additional file 1: Fig. S8 C, D). Different from the above findings in mouse embryos, we observed similar chromatin interaction frequencies in untreated and CX-5461-treated human embryos (Fig. 4E, Additional file 1: Fig. S8E). Further genome-wide TAD normalization analysis showed CX- 5461 treatment did not disturb the TAD strength during human embryonic development (Fig. 4F). Furthermore, the scaling of contact frequencies as a function of genomic separation was unchanged (Fig. 4G), and there was a consistent trend of chromatin interactions between CX- 5461-treated human embryos and the control group at the whole genome level (Additional file 1:

(See figure on next page.)

Fig. 4 Changes of the TAD structure in mouse and human embryos after inhibiting Pol I transcription. **A** Interaction frequency heatmap of mouse early embryos at a 25 kb resolution. **B** Genome-wide TAD signals in mouse 2-Cell, mouse 2-Cell_α-amanitin, and mouse 2-Cell_CX5461 groups. **C** Average contact probability across the genome was decreased as a function of genomic distance in 2-Cell, 2-Cell_α-amanitin, and 2-Cell_CX5461 groups in mouse. **D** Ratio of total interactions between genomic distances of >2 Mb and ≤2 Mb in mouse (Wilcox test, ns: $p>0.05$). **E** Interaction frequency heatmap of human early embryos at a 25 kb resolution. **F** Genome-wide TAD signals in human 4-Cell, human 8-Cell, and human 8-Cell_CX5461 groups. **G** Average contact probability across the genome was decreased as a function of genomic distance in 2-Cell, 2-Cell_α-amanitin, and 2-Cell_CX5461 groups in human. **H** Ratio of total interactions between genomic distances of >2 Mb and ≤2 Mb in humans (Wilcox test, ns: $p>0.05$)

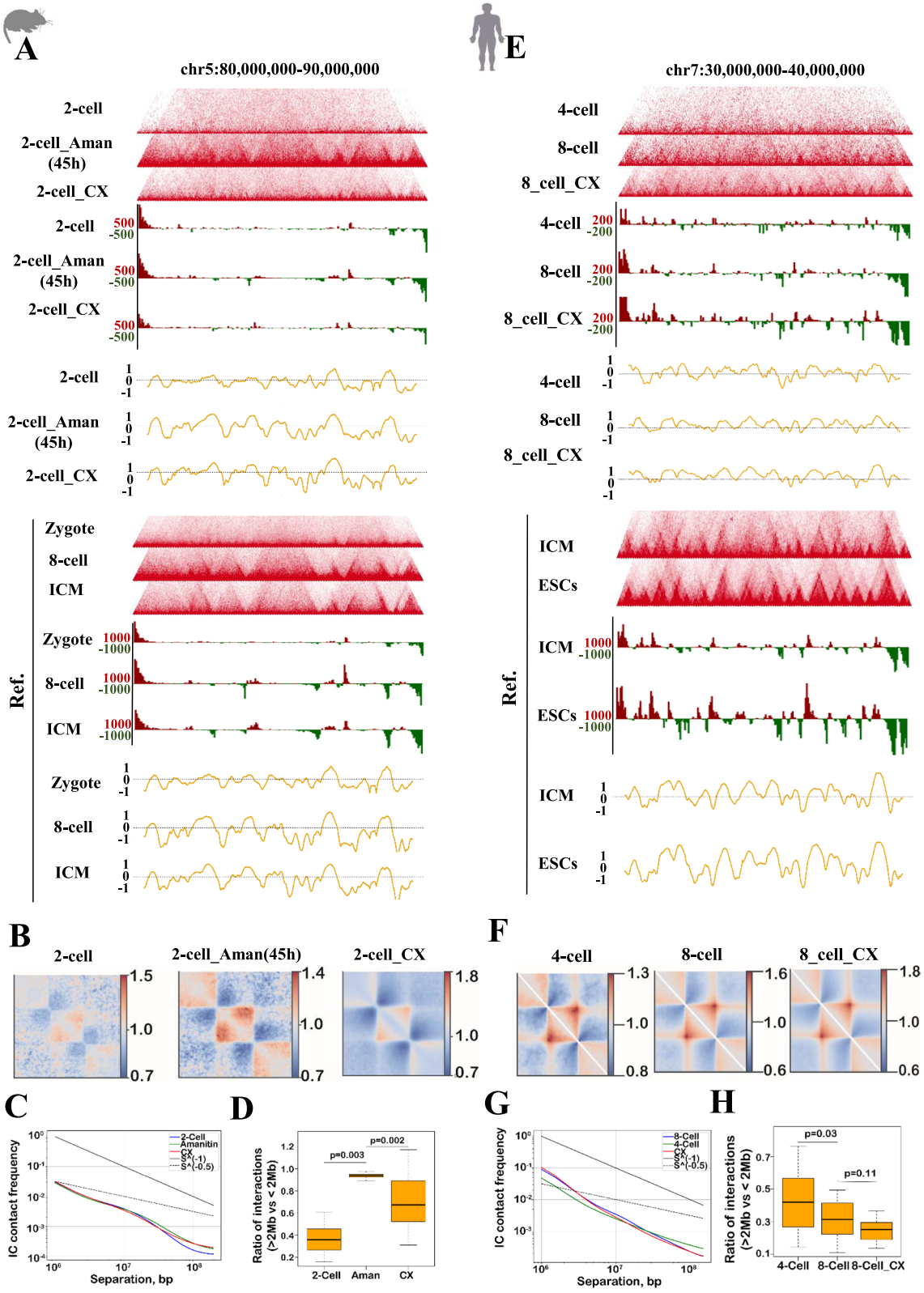

Fig. 4 (See legend on previous page.)

Fig. S8 F). Statistical analysis also showed no significant difference in the ratio of interactions outside 2 Mb and interactions within a 2-Mb distance between control and treated groups (Fig. 4H). Taken together, these data show that inhibition of Pol I transcription prevents re-establishment of the TAD structure in mouse early embryos, but not in human embryos.

Pol I transcription plays an opposing role in maintenance of chromatin structures between human and mouse FGSCs

Next, we determined whether Pol I transcription plays a role in maintaining the chromatin structure. We found that CX- 5461-treated FGSCs became significantly enlarged (Fig. 5A and Additional file 1: Fig. S9 A-D). Furthermore, CCK- 8, EdU, and flow cytometric assays showed decreases in cell activity and proliferation rates (Fig. 5B, C and Additional file 1: Fig. S9E, F). Additionally, expression of meiotic markers *Stra8* and *Sycp3* was upregulated after CX- 5461 treatment (Additional file 1: Fig. S9G,H). These results suggest that inhibition of Pol I transcription reduces mFGSC proliferation and promotes their differentiation. Unlike mFGSCs, inhibition of Pol I transcription in hFGSCs reduced cell activity and proliferation, but did not promote their differentiation (Figs. 5 D–F and Additional file 1: Fig. S10 A-F).

Hi-C contact maps showed that inhibition of Pol I transcription had different effects on the interaction frequency between human and mouse FGSCs (Fig. 5G, H and Additional file 1: Fig. S11 A, B). Hi-C contact maps showed that the interaction frequency in CX- 5461-treated mFGSCs was lower than that in untreated mFGSCs (Fig. 5I). However, the interaction frequency in CX- 5461-treated hFGSCs was higher than that in untreated hFGSCs (Fig. 5J). Additionally, CX-5461-treated mFGSCs had a lower interaction frequency than untreated mFGSCs at a distance of ≤2 Mb. Conversely, CX- 5461-treated hFGSCs had a high interaction frequency at a distance of ≤2 Mb (Additional file 1: Fig. S11 C, D). Corresponding to this finding, the ratio of genomic distance >2 Mb versus ≤2 Mb was lower in CX- 5461-treated hFGSCs (Additional file 1: Fig. S11 F). However, there was no difference in the ratio of genomic distance >2 Mb versus ≤2 Mb between CX- 5461-treated mFGSCs and controls (Additional file 1: Fig. S11E). Collectively, these results demonstrated that Pol transcription has opposing effects on global reorganization of the chromatin structure between mFGSCs and hFGSCs.

Analysis of the TAD structure showed that DI values in CX- 5461-treated mFGSCs were lower than those in controls (Additional file 1: Fig. S11G). Consistently, the triangular structures of TADs in CX- 5461-treated mFGSCs were not as clear as those in controls (Fig. 5G). Relative variance of the TAD signal and TAD boundary strength in CX- 5461-treated mFGSCs were also significantly lower than that in controls (Fig. 5K and Additional file 1: Fig. S12A). Conversely, the absolute DI value, TAD signal, and TAD boundary in CX- 5461-treated hFGSCs were higher than those in controls (Fig. 5L and Additional file 1: Fig. S11H, Fig. S12B). Additionally, genome-wide statistical analysis showed that the interaction within TADs was reduced in CX- 5461-treated mFGSCs, but it enhanced in CX- 5461-treated hFGSCs (Fig. 5M, N). These results indicate that Pol I transcription plays distinct roles in maintenance of the TAD structure in hFGSCs and mFGSCs. Integrative analysis of Hi-C and CTCF ChIP-seq data showed that the boundary strength of TADs with or without CTCF binding was reduced, indicating that Pol I transcription has a genome-wide effect on the TAD structure (Additional file 1: Fig. S12 C). Interestingly, there was no significant difference in compartment strengths of the A/B region in CX-5461-treated mFGSCs and hFGSCs (Additional file 1: Fig. S12D, E). Overall, these results demonstrate that inhibition of Pol I transcription enhances the TAD structure in hFGSCs, but weakens the TAD structure in mFGSCs.

Discussion

We systematically revealed that the 3D chromatin structure undergoes extensive reprogramming from human gametogenesis to early embryonic development. During oogenesis, the TAD structure showed a weakening trend and essentially disappeared in hGV oocytes, which was different from the visible TAD structure in mGV oocytes.

(See figure on next page.)

Fig. 5 Effect of RNA transcription on chromatin structures in mouse and human FGSCs. **A** Morphological changes of mFGSCs before and after CX-5461 treatment. Scale bar, 50 μm. **B** mFGSC proliferation was assessed by EdU assays. **C** mFGSC viability was assessed by CCK-8 assays (Students' *t* test, ***$p<0.001$). **D** Morphological changes of hFGSCs before and after CX-5461 treatment. Scale bar, 50 μm. **E** hFGSC proliferation was assessed by EdU assays. **F** hFGSC viability was assessed by CCK-8 assays (Students' *t* test, ***$p<0.001$). **G,H** Standardized Hi-C interaction heatmap, directional indexes (DIs), and first principal component (PC1) values in mice (**G**) and humans (**H**) at a 40 kb resolution. **I, J** Average contact probability across the genome decreases as a function of genomic distance in mice (**I**) and humans (**J**). **K, L** Box plot showing the change in the TAD boundary intensity before and after Pol I transcriptional inhibition in mouse (**K**) and human FGSCs (**L**) (Wilcox test, **$p<0.01$, ***$p<0.001$). **M, N** Representative region showing the chromatin interaction within the TAD structure at a 40 kb resolution in mouse (**M**) and human FGSCs (**N**) between control and treatment

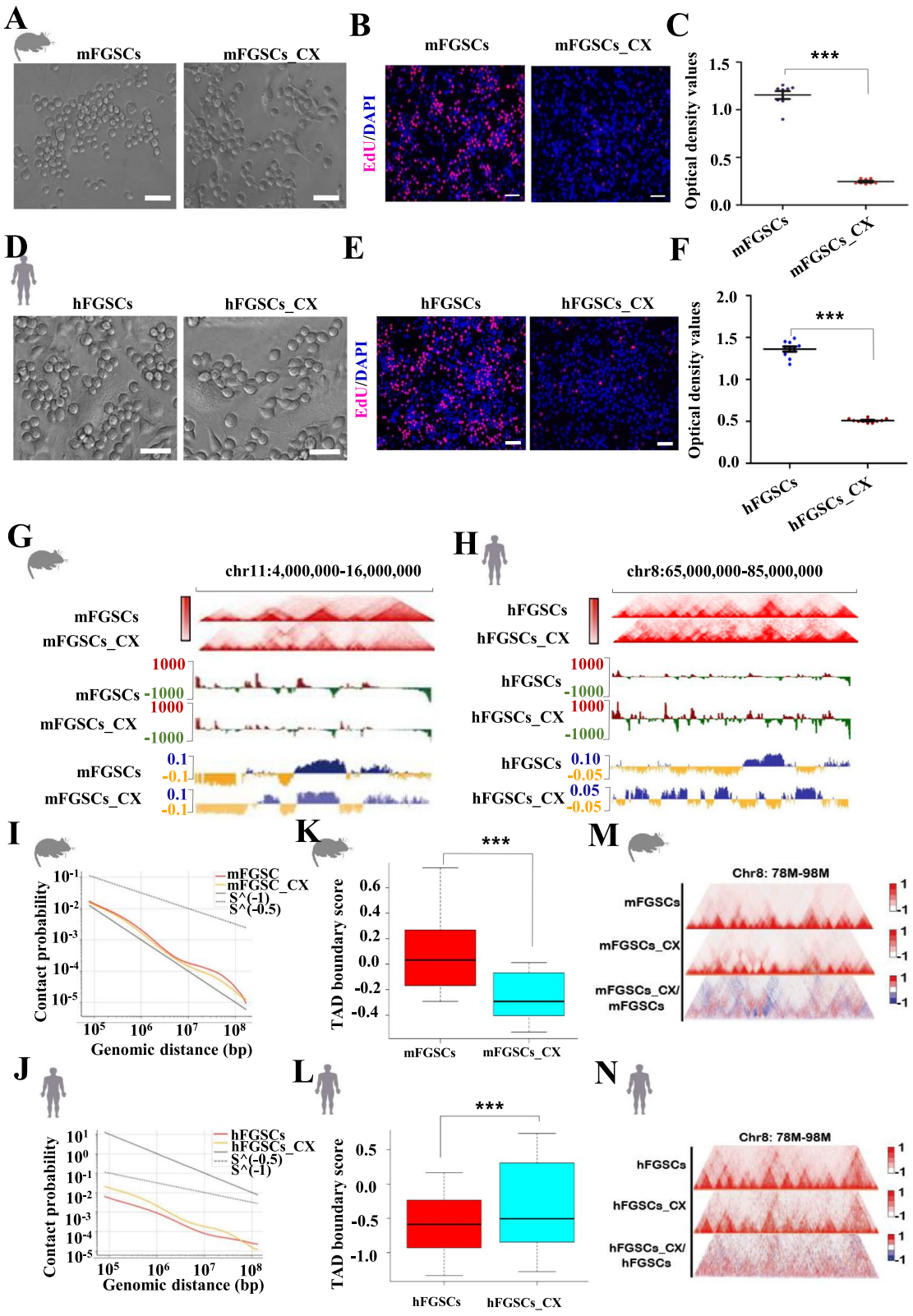

Fig. 5 (See legend on previous page.)

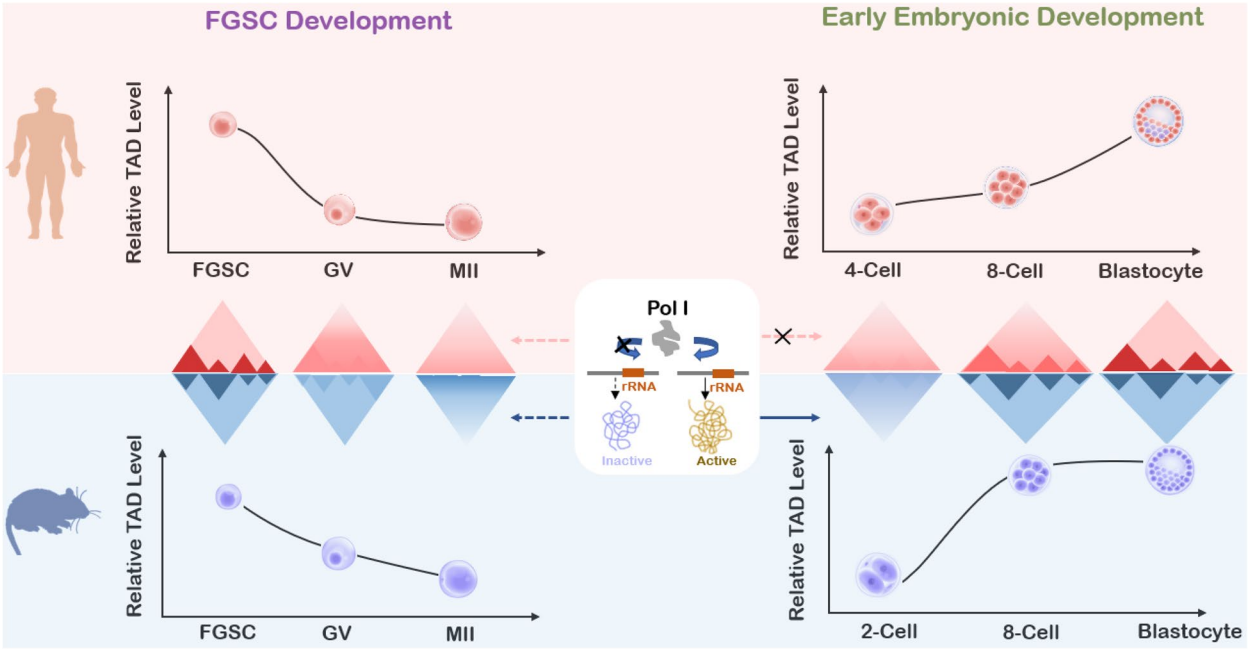

Fig. 6 Graph of Pol I function of 3D genome in FGSC development and early embryonic development between mouse and human

After fertilization, the TAD structure re-established from the human 4-cell to 8-cell embryo.

Consistent with previous observations in mouse sperm, our analysis revealed a high frequency of inter-chromosomal interactions and extensive long-range intra-chromosomal contacts in human sperm chromatin [14, 15]. This characteristic chromatin organization pattern appears to be evolutionarily conserved, as similar features have been documented in rhesus monkey spermatogenesis [14]. In contrast to a previous study by Chen et al. [18], we detected distinct A/B compartments and TAD structures in human sperm. These disparate findings might be attributed to several technical factors, including differences in sequencing depth, computational analysis pipelines, and sample heterogeneity. Notably, Chen et al. hypothesized that the absence of TAD structures was due to the lack of CTCF expression in sperm cells. However, recent single-cell RNA-sequencing data have demonstrated detectable CTCF expression in human sperm [57]. This suggests that the discrepancies in observed TAD structures may be related to varying levels of CTCF expression among different sperm populations, rather than a complete absence of this crucial architectural protein.

Chromatin organization plays an important role in regulating spatiotemporal transcription of genes during development [58, 59], and disruption of the TAD boundary leads to abnormal development [60]. Furthermore, deletions, inversions, or duplications of the TAD structure cause human limb malformations [60], indicating the functional importance of TADs for development. In various animals, the timing of TAD structure establishment is different [11, 12, 17]. In zebrafish embryos, the TAD structure is detectable before ZGA [61]. Whereas in drosophila embryos, the TAD structure is established at the onset of ZGA [17]. By comparing the chromatin structure dynamics between human and mouse embryos, we found both conservation and divergence in the chromatin structures. More importantly, TAD structures are gradually established in both humans and mice during ZGA. ZGA is an important event for early embryonic development, which is mainly transcribed by three RNA polymerases, Pol I–III [62]. Hence, establishment of the TAD structure may be associated with transcription of RNA polymerase. To clarify the role of RNA polymerase in establishment of the chromatin structure, we analyzed single-cell transcriptome data of embryos at various developmental stages [53]. The analysis revealed a dramatic increase in Pol II transcriptional activity during the transition from 4-cell to 8-cell stage in human embryos, coinciding with TAD structure establishment dependent on Pol II transcription [18]. Intriguingly, in mouse embryos, we observed a sharp increase in Pol I, rather than Pol II, transcription during the transition from early to late 2-cell stage. This observation aligned with the developmental arrest at the 2-cell stage following Pol I knockdown or inhibition. To further investigate this phenomenon, we performed Hi-C analysis

on mouse embryos treated with a Pol I inhibitor. Our results demonstrated that Pol I transcription inhibition prevented TAD structure establishment specifically in mouse embryos, while human embryos remained unaffected. Notably, RNA-seq analysis of Pol I-inhibited embryos revealed significant alterations in the expression of key chromatin regulators, including TRIM28, OCT4, and HDAC1, leading to chromatin silencing. The involvement of TRIM28, a well-established heterochromatin marker, suggests that rRNA transcription modulates chromatin structure through regulation of epigenetic states in specific chromatin regions, consistent with previous report [63].

Interestingly, inhibition of Pol I transcription reduced mFGSC proliferation and promoted their differentiation, whereas inhibition of Pol I transcription in hFGSCs reduced cell activity and proliferation, but did not promote their differentiation. Furthermore, the TAD structure in mFGSCs was significantly weakened after inhibition of Pol I transcription. Conversely, the TAD structure and contact probability in hFGSCs were enhanced after inhibition of Pol I transcription. These findings suggest that Pol I transcription plays various roles in maintaining chromatin structures between hFGSCs and mFGSCs.

In summary, we systematically analyzed the landscape of the chromatin structure from human gametogenesis to early embryonic development (Fig. 6). Furthermore, by comparing the divergence in the chromatin structure between human and mouse embryos at various development stages, we revealed that Pol I transcription plays a critical role in establishment of the TAD structure in mouse embryos. These findings provide a valuable resource for future studies of chromatin organization during germ cell and embryonic development, and are of great significance to maintain fertility and prevent birth defects.

Conclusions

Our comparative analysis reveals fundamental differences in 3D genome reorganization between human and mouse gametogenesis and early embryogenesis, with chromatin architecture establishment initiating at the 4-cell stage in humans versus the 2-cell stage in mice. We demonstrate that Pol I serves as a species-specific regulator of TAD formation, which is essential for chromatin organization in mouse embryos but dispensable in human embryos. Intriguingly, we uncover opposing roles for Pol I in TAD regulation, where its inhibition strengthens TADs in hFGSCs while weakening them in mFGSCs. These findings provide novel mechanistic insights into the evolutionary divergence of chromatin architecture regulation during early mammalian development. Our integrated multi-omics approach establishes Pol I-mediated chromatin organization as a previously unrecognized aspect of species-specific developmental control, advancing both fundamental understanding of 3D genome dynamics and potential applications in reproductive medicine.

Supplementary Information

The online version contains supplementary material available at https://doi.org/10.1186/s13073-025-01476-y.

Additional file 1: Supplementary figure and figure legends. Figure S1. Biological characteristics of human germ stem cells and early embryos. Figure S2. Validation of Hi-C data. Figure S3. Features of chromatin organization during FGSC development. Figure S4. Changes in the TAD structure and A/B compartment in hSSCs and sperm. Figure S5. Overall chromosome organization during human early embryonic development. Figure S6. Chromatin landscapes vary in humans and mice during FGSC development. Figure S7. Comparison of the higher order chromatin organization between human and mouse embryos. Figure S8. Effect of POLR1A knockdown on the development of early mouse embryos. Figure S9. Changes of chromatin interactions in mouse and human embryos after treatment with Pol I inhibitors. Figure S10. Effect of Pol I transcription on self-renewal and differentiation of mFGSCs. Figure S11. Effect of Pol I transcription on hFGSCs proliferation. Figure S12. Global chromatin structure of human and mouse FGSCs after the inhibition of Pol I transcription. Figure S13. Changes in the TAD structure in human and mouse FGSCs after inhibition of Pol I transcription.

Additional file 2: Table S1. The summary of Hi-C experiment reads.

Additional file 3: Table S2. The sequence of primer for RT-PCR.

Additional file 4: Table S3. The gene list of ZGA and housekeeping genes.

Acknowledgements
Not applicable

Authors' contributions
C.H, G.G.T, S.H, B.C, X.L, B.X, and Y.C contributed equally to this work. C.H performed the Hi-C experiments and Pol I-related experiments. G.G.T conducted all data analysis. C.H, G.G.T, and J.W wrote the manuscript. S.H, B.C, and B.X collected part of human oocytes and human embryos and did related experiments. X.L collected the hFGSCs and characterization of hFGSCs. W. L collected human testis tissues. R.H, H.C, Y.Z, M.Z, Z.W, Z.Z, and J.Z performed the embryo manipulation experiments. Z.W, G.Y, and P.Y collected part of human oocytes. X.T, Q.F collected human sperm, human ovarian tissues, and part of human embryos. Y.C performed the Hi-C experiments of 2-Cell and 2-Cell_α-amanitin group. Y.W and Y.G help to improve the Hi-C experiments. G.T, X.T, Y.S, and Y.C were concerned this project. J.W, G.G.T, and C.H designed this study. W.J supervised the study. All authors read and approved the final manuscript.

Funding
This work was supported by National key research and development program of China (2022YFA0806301), National Nature Science Foundation of China (82201780), the Scientific and Technological Innovation Action program of Shanghai (23 JC1402800), and Shanghai Jiao Tong University 2030 Initiative. National Key Research and Development Program of China,2022YFA0806301,Ji Wu,National Nature Science Foundation of China,82201780,Geng G. Tian,the Scientific and Technological Innovation Action program of Shanghai,23 JC1402800,Ji Wu

Data availability
The mouse embryos Hi-C data were downloaded from published article: Du Z, Zheng H, Huang B, et al. Allelic reprogramming of 3D chromatin architecture during early mammalian development. PRJNA326112, NCBI Sequence Read Archive. 2017. (https://www.ncbi.nlm.nih.gov/bioproject/PRJNA326112) [39]. The human embryos RNA-seq data were downloaded from published article: Yan L, Yang M, Guo H, et al. Single-cell RNA-Seq profiling of human preimplantation embryos and embryonic stem cells. PRJNA153427, NCBI

Sequence Read Archive. 2013. (https://www.ncbi.nlm.nih.gov/bioproject/PRJNA153427) [53]. The mouse embryos RNA-seq data were downloaded from published article: Wu J, Huang B, Chen H, et al. The landscape of accessible chromatin in mammalian preimplantation embryos. PRJNA277361, NCBI Sequence Read Archive. 2016. (https://www.ncbi.nlm.nih.gov/bioproject/PRJNA277361) [54]. The human embryos Hi-C raw sequence data are available from the China National Center for Bioinformation, National Genomics Data Center under accession number PRJCA016057 HRA004381 (https://bigd.big.ac.cn/gsa-human/browse/HRA004381) [64] and CRA010655 (https://ngdc.cncb.ac.cn/gsa/browse/CRA010655) [65] for mouse CX-5461-treated Hi-C data, mouse embryos RNA-seq, and Pol I ChIP-seq data are available from Gene Expression Omnibus (GEO) under the accession number: PRJNA989148 GSE236161 (https://www.ncbi.nlm.nih.gov/geo/query/acc.cgi?acc=GSE236161) [66].

Declarations

Ethics approval and consent to participate

This study was approved by the institutional review boards of The Affiliated Ren Ji Hospital of Shanghai Jiao Tong University (2019122701), Affiliated Tongji Hospital of Tongji University (2020-KYSB- 048), Shanghai First Maternity, and Infant Hospital (KS21280), The First Affiliated Hospital of Anhui Medical University (2020H026), and Shuguang Hospital Affiliated to Shanghai University of Traditional Chinese Medicine (2020–866 - 75–01). The study was conducted in accordance with the measures of the People's Republic of China on the administration of human-assisted reproductive technology, the ethical principles of human-assisted reproductive technology, and the Helsinki Declaration. All participants provided written informed consent to participate in the study. All animal experiments were conducted in accordance with the recommendations of the Guide for the Care and Use of Laboratory Animals and relevant Chinese laws and regulations, and were approved by the Institutional Animal Care and Use Committee (IACUC) of Shanghai Jiao Tong University (Spatiotemporal dynamics and regulatory mechanisms of gametogenesis and embryonic development in mammals, A2019118).

Competing interests

The authors declare that they have no competing interests.

Author details

[1]Key Laboratory for the Genetics of Developmental & Neuropsychiatric Disorders (Ministry of Education), Bio-X Institutes, School of Medicine, Shanghai Jiao Tong University, Shanghai, China. [2]Shanghai Key Laboratory of Veterinary Biotechnology, School of Agriculture and Biology, Shanghai Jiao Tong University, Shanghai 200240, China. [3]Center for Reproductive Medicine, Renji Hospital, Shanghai Jiao Tong University School of Medicine, Shanghai 200135, China. [4]Shanghai Key Laboratory for Assisted Reproduction and Reproductive Genetics, Shanghai, China. [5]Department of Obstetrics and Gynecology, Reproductive Medicine Center, The First Affiliated Hospital of Anhui Medical University, Hefei, China. [6]Department of Urology, Tongji Hospital, Tongji University School of Medicine, 389 Xincun Road, Shanghai, China. [7]Ningxia Key Laboratory of Clinical and Pathogenic Microbiology, Institute of Medical Sciences, General Hospital of Ningxia Medical University, Yinchuan, China. [8]Institute of Reproductive Medicine, Medical School of Nantong University, Nantong, China. [9]National Laboratory of Macromolecules, Institute of Biophysics, Chinese Academy of Sciences, Beijing, China. [10]Laboratory Animal Center, Instrumental Analysis Center, Shanghai Jiao Tong University, Shanghai, China. [11]Department of Reproductive Medicine, Guanghua HospitalAffiliated to, Shanghai University of Traditional Chinese Medicine, 540 Xinhua Road, Shanghai, China. [12]Sheng Yushou Center of Cell Biology and Immunology , School of Life Sciences and Biotechnology, Shanghai Jiao Tong University, Shanghai 200240, China. [13]Shuguang Hospital affiliated to, Shanghai University of Traditional Chinese Medicine, Shanghai, China. [14]Department of Reproductive Medicine, The First Affiliated Hospital of Xi'an Jiao Tong University, Xi'an, China. [15]Department of Assisted Reproduction, Shanghai First Maternity and Infant Hospital, School of Medicine, Tongji University, Shanghai, China. [16]Key Laboratory of Fertility Preservation and Maintenance of Ministry of Education, Ningxia Medical University, Yinchuan, China.

Received: 23 July 2023 Accepted: 21 April 2025
Published online: 19 May 2025

References

1. Pope BD, Ryba T, Dileep V, Yue F, Wu W, Denas O, Vera DL, Wang Y, Hansen RS, Canfield TK, et al. Topologically associating domains are stable units of replication-timing regulation. Nature. 2014;515(7527):402–5.
2. Lieberman-Aiden E, van Berkum NL, Williams L, Imakaev M, Ragoczy T, Telling A, Amit I, Lajoie BR, Sabo PJ, Dorschner MO, et al. Comprehensive mapping of long-range interactions reveals folding principles of the human genome. Science. 2009;326(5950):289–93.
3. Nora EP, Lajoie BR, Schulz EG, Giorgetti L, Okamoto I, Servant N, Piolot T, van Berkum NL, Meisig J, Sedat J, et al. Spatial partitioning of the regulatory landscape of the X-inactivation centre. Nature. 2012;485(7398):381–5.
4. Bonev B, Mendelson Cohen N, Szabo Q, Fritsch L, Papadopoulos GL, Lubling Y, Xu X, Lv X, Hugnot JP, Tanay A, Cavalli G. Multiscale 3D genome rewiring during mouse neural development. Cell. 2017;171(3):557–72.
5. Rao SSP, Huntley MH, Durand NC, Stamenova EK, Bochkov ID, Robinson JT, Sanborn AL, Machol I, Omer AD, Lander ES. A 3D map of the human genome at kilobase resolution reveals principles of chromatin looping. Cell. 2014;159(7):1665–80.
6. Wang XQD, Dostie J. Chromosome folding and its regulation in health and disease. Curr Opin Genet Dev. 2017;43:23–30.
7. Dixon JR, Jung I, Selvaraj S, Shen Y, Antosiewicz-Bourget JE, Lee AY, Ye Z, Kim A, Rajagopal N, Xie W, et al. Chromatin architecture reorganization during stem cell differentiation. Nature. 2015;518(7539):331–6.
8. Du Z, Zheng H, Kawamura YK, Zhang K, Gassler J, Powell S, Xu Q, Lin Z, Xu K, Zhou Q, et al. Polycomb group proteins regulate chromatin architecture in mouse oocytes and early embryos. Mol Cell. 2019;77(4):825–39.
9. Tian GG, Hou C, Li J, Wu J. Three-dimensional genome structure shapes the recombination landscape of chromatin features during female germline stem cell development. Clin Transl Med. 2022;12(6): e927.
10. Flyamer IM, Gassler J, Imakaev M, Brandao HB, Ulianov SV, Abdennur N, Razin SV, Mirny LA, Tachibana-Konwalski K. Single-nucleus Hi-C reveals unique chromatin reorganization at oocyte-to-zygote transition. Nature. 2017;544(7648):110–4.
11. Du Z, Zheng H, Huang B, Ma R, Wu J, Zhang X, He J, Xiang Y, Wang Q, Li Y, et al. Allelic reprogramming of 3D chromatin architecture during early mammalian development. Nature. 2017;547(7662):232–5.
12. Ke Y, Xu Y, Chen X, Feng S, Liu Z, Sun Y, Yao X, Li F, Zhu W, Gao L, et al. 3D chromatin structures of mature gametes and structural reprogramming during mammalian embryogenesis. Cell. 2017;170(2):367–81.
13. Vara C, Paytuvi-Gallart A, Cuartero Y, Le Dily F, Garcia F, Salva-Castro J, Gomez HL, Julia E, Moutinho C, Aiese Cigliano R, et al. Three-dimensional genomic structure and cohesin occupancy correlate with transcriptional activity during spermatogenesis. Cell Rep. 2019;28(2):352–67.
14. Wang Y, Wang H, Zhang Y, Du Z, Si W, Fan S, Qin D, Wang M, Duan Y, Li L, et al. Reprogramming of meiotic chromatin architecture during spermatogenesis. Mol Cell. 2019;73(3):547–61.
15. Battulin N, Fishman VS, Mazur AM, Pomaznoy M, Khabarova AA, Afonnikov DA, Prokhortchouk EB, Serov OL. Comparison of the three-dimensional organization of sperm and fibroblast genomes using the Hi-C approach. Genome Biol. 2015;16(1):77.
16. Jung YH, Sauria MEG, Lyu X, Cheema MS, Ausio J, Taylor J, Corces VG. Chromatin states in mouse sperm correlate with embryonic and adult regulatory landscapes. Cell Rep. 2017;18(6):1366–82.
17. Hug CB, Grimaldi AG, Kruse K, Vaquerizas JM. Chromatin architecture emerges during zygotic genome activation independent of transcription. Cell. 2017;169(2):216–28.
18. Chen X, Ke Y, Wu K, Zhao H, Sun Y, Gao L, Liu Z, Zhang J, Tao W, Hou Z, et al. Key role for CTCF in establishing chromatin structure in human embryos. Nature. 2019;576(7786):306–10.
19. Borsos M, Perricone SM, Schauer T, Pontabry J, de Luca KL, de Vries SS, Ruiz-Morales ER, Torres-Padilla ME, Kind J. Genome-lamina interactions are established de novo in the early mouse embryo. Nature. 2019;569(7758):729–33.
20. Rowley MJ, Nichols MH, Lyu X, Ando-Kuri M, Rivera ISM, Hermetz K, Wang P, Ruan Y, Corces VG. Evolutionarily conserved principles predict 3D chromatin organization. Mol Cell. 2017;67(5):837–52.
21. Chu C, Qu K, Zhong FL, Artandi SE, Chang HY. Genomic maps of long noncoding RNA occupancy reveal principles of RNA-chromatin interactions. Mol Cell. 2011;44(4):667–78.
22. Cramer P, Armache KJ, Baumli S, Benkert S, Brueckner F, Buchen C, Damsma GE, Dengl S, Geiger SR, Jasiak AJ, et al. Structure of eukaryotic RNA polymerases. Annu Rev Biophys. 2008;37:337–52.

23. Song CZ, Hanada K, Yano K, Maeda Y, Yamamoto K, Muramatsu M. High conservation of subunit composition of RNA polymerase I(A) between yeast and mouse and the molecular cloning of mouse RNA polymerase I 40-kDa subunit RPA40. J Biol Chem. 1994;269(43):26976–81.
24. Jorgensen P, Rupes I, Sharom JR, Schneper L, Broach JR, Tyers M. A dynamic transcriptional network communicates growth potential to ribosome synthesis and critical cell size. Genes Dev. 2004;18(20):2491–505.
25. Warner JR. The economics of ribosome biosynthesis in yeast. Trends Biochem Sci. 1999;24(11):437–40.
26. Yao RW, Xu G, Wang Y, Shan L, Luan PF, Wang Y, Wu M, Yang LZ, Xing YH, Yang L, Chen LL. Nascent pre-rRNA sorting via phase separation drives the assembly of dense fibrillar components in the human nucleolus. Mol Cell. 2019;76(5):767–83.
27. Scheer U, Benavente R. Functional and dynamic aspects of the mammalian nucleolus. BioEssays. 1990;12(1):14–21.
28. Benavente R, Reimer G, Rose KM, Hügle-Dörr B, Scheer U. Nucleolar changes after microinjection of antibodies to RNA polymerase I into the nucleus of mammalian cells. Chromosoma. 1988;97(2):115–23.
29. Angelov D, Bondarenko VA, Almagro S, Menoni H, Mongélard F, Hans F, Mietton F, Studitsky VM, Hamiche A, Dimitrov S, Bouvet P. Nucleolin is a histone chaperone with FACT-like activity and assists remodeling of nucleosomes. Embo j. 2006;25(8):1669–79.
30. De La Fuente R. Chromatin modifications in the germinal vesicle (GV) of mammalian oocytes. Dev Biol. 2006;292(1):1–12.
31. Shishova KV, Lavrentyeva EA, Dobrucki JW, Zatsepina OV. Nucleolus-like bodies of fully-grown mouse oocytes contain key nucleolar proteins but are impoverished for rRNA. Dev Biol. 2015;397(2):267–81.
32. Wang QT, Piotrowska K, Ciemerych MA, Milenkovic L, Scott MP, Davis RW, Zernicka-Goetz M. A genome-wide study of gene activity reveals developmental signaling pathways in the preimplantation mouse embryo. Dev Cell. 2004;6(1):133–44.
33. Zeng F, Baldwin DA, Schultz RM. Transcript profiling during preimplantation mouse development. Dev Biol. 2004;272(2):483–96.
34. Ding X, Liu G, Xu B, Wu C, Hui N, Ni X, Wang J, Du M, Teng X, Wu J. Human GV oocytes generated by mitotically active germ cells obtained from follicular aspirates. Sci Rep. 2016;6:28218.
35. Zou K, Yuan Z, Yang Z, Luo H, Sun K, Zhou L, Xiang J, Shi L, Yu Q, Zhang Y, et al. Production of offspring from a germline stem cell line derived from neonatal ovaries. Nat Cell Biol. 2009;11(5):631–6.
36. Wu C, Xu B, Li X, Ma W, Zhang P, Chen X, Wu J. Tracing and characterizing the development of transplanted female germline stem cells in vivo. Mol Ther. 2017;25(6):1408–19.
37. Hou C, Zhao X, Tian GG, Wu J. Stella regulates the development of female germline stem cells by modulating chromatin structure and DNA methylation. Int J Biol Sci. 2022;18(7):3006–18.
38. Zhang YL, Zhao LW, Zhang J, Le R, Ji SY, Chen C, Gao Y, Li D, Gao S, Fan HY. DCAF13 promotes pluripotency by negatively regulating SUV39H1 stability during early embryonic development. EMBO J. 2018;37(18): e98981.
39. Du Z, Zheng H, Huang B, et al. Allelic reprogramming of 3D chromatin architecture during early mammalian development. PRJNA326112, NCBI Sequence Read Archive. 2017. https://www.ncbi.nlm.nih.gov/bioproject/PRJNA326112 . Cited 2025 Apr 25.
40. Tian GG, Zhao X, Hou C, Xie W, Li X, Wang Y, Wang L, Li H, Zhao X, Li J. Integrative analysis of the 3D genome structure reveals that CTCF maintains the properties of mouse female germline stem cells. Cell Mol Life Sci. 2022;79(1):22.
41. Picelli S, Faridani OR, Björklund AK, Winberg G, Sagasser S, Sandberg R. Full-length RNA-seq from single cells using Smart-seq2. Nat Protoc. 2014;9(1):171–81.
42. Hu Y, Huang K, An Q, Du G, Hu G, Xue J, Zhu X, Wang CY, Xue Z, Fan G. Simultaneous profiling of transcriptome and DNA methylome from a single cell. Genome Biol. 2016;17:88.
43. Wang Y, Liu L, Song Y, Yu X, Deng H. Unveiling E2F4, TEAD1 and AP-1 as regulatory transcription factors of the replicative senescence program by multi-omics analysis. Protein Cell. 2022;13(10):742–59.
44. Tian GG, Li J, Wu J. Comparison analysis of multiple-omics data between female germline stem cells and spermatogonial stem cells. Genes & Diseases. 2023;10(3):727–30.
45. Yang T, Zhang F, Yardımcı GG, Song F, Hardison RC, Noble WS, Yue F, Li Q. HiCRep: assessing the reproducibility of Hi-C data using a stratum-adjusted correlation coefficient. Genome Res. 2017;27(11):1939–49.
46. Crane E, Bian Q, McCord RP, Lajoie BR, Wheeler BS, Ralston EJ, Uzawa S, Dekker J, Meyer BJ. Condensin-driven remodelling of X chromosome topology during dosage compensation. Nature. 2015;523(7559):240–4.
47. Yu G, Wang L-G, Han Y, He Q-Y. clusterProfiler: an R package for comparing biological themes among gene clusters. Omics: a journal of integrative biology. 2012;16(5):284–7.
48. Zhang Y, Liu T, Meyer CA, Eeckhoute J, Johnson DS, Bernstein BE, Nusbaum C, Myers RM, Brown M, Li W. Model-based analysis of ChIP-Seq (MACS). Genome Biol. 2008;9(9):1–9.
49. Stark R, Brown G. DiffBind: differential binding analysis of ChIP-Seq peak data. R package version. 2011;100(4.3):2–21.
50. Ramírez F, Dündar F, Diehl S, Grüning BA, Manke T. deepTools: a flexible platform for exploring deep-sequencing data. Nucleic Acids Res. 2014;42(W1):W187–91.
51. McLean CY, Bristor D, Hiller M, Clarke SL, Schaar BT, Lowe CB, Wenger AM, Bejerano G. GREAT improves functional interpretation of cis-regulatory regions. Nat Biotechnol. 2010;28(5):495–501.
52. Naumova N, Imakaev M, Fudenberg G, Zhan Y, Lajoie BR, Mirny LA, Dekker J. Organization of the mitotic chromosome. Science. 2013;342(6161):948–53.
53. Yan L, Yang M, Guo H, et al. Single-cell RNA-Seq profiling of human preimplantation embryos and embryonic stem cells. PRJNA153427, NCBI Sequence Read Archive. 2013. https://www.ncbi.nlm.nih.gov/bioproject/PRJNA153427 . Cited 2025 Apr 25.
54. Wu J, Huang B, Chen H, et al. The landscape of accessible chromatin in mammalian preimplantation embryos. PRJNA277361, NCBI Sequence Read Archive. 2016. https://www.ncbi.nlm.nih.gov/bioproject/PRJNA277361 . Cited 2025 Apr 25.
55. Lin CJ, Koh FM, Wong P, Conti M, Ramalho-Santos M. Hira-mediated H3.3 incorporation is required for DNA replication and ribosomal RNA transcription in the mouse zygote. Dev Cell. 2014;30(3):268–79.
56. Laferte A, Favry E, Sentenac A, Riva M, Carles C, Chedin S. The transcriptional activity of RNA polymerase I is a key determinant for the level of all ribosome components. Genes Dev. 2006;20(15):2030–40.
57. Wang M, Liu X, Chang G, Chen Y, An G, Yan L, Gao S, Xu Y, Cui Y, Dong J, et al. Single-cell RNA sequencing analysis reveals sequential cell fate transition during human spermatogenesis. Cell Stem Cell. 2018;23(4):599–614.
58. Bushey AM, Dorman ER, Corces VG. Chromatin insulators: regulatory mechanisms and epigenetic inheritance. Mol Cell. 2008;32(1):1–9.
59. Phillips JE, Corces VG. CTCF: master weaver of the genome. Cell. 2009;137(7):1194–211.
60. Lupianez DG, Kraft K, Heinrich V, Krawitz P, Brancati F, Klopocki E, Horn D, Kayserili H, Opitz JM, Laxova R, et al. Disruptions of topological chromatin domains cause pathogenic rewiring of gene-enhancer interactions. Cell. 2015;161(5):1012–25.
61. Kaaij LJT, van der Weide RH, Ketting RF, de Wit E. Systemic loss and gain of chromatin architecture throughout zebrafish development. Cell Rep. 2018;24(1):1–10.
62. Svoboda P. Mammalian zygotic genome activation. Semin Cell Dev Biol. 2018;84:118–26.
63. Yu H, Sun Z, Tan T, Pan H, Zhao J, Zhang L, Chen J, Lei A, Zhu Y, Chen L, et al. rRNA biogenesis regulates mouse 2C-like state by 3D structure reorganization of peri-nucleolar heterochromatin. Nat Commun. 2021;12(1):6365.
64. Hou C, Tian GG, Hu S, et al. RNA polymerase I is essential for driving the formation of 3D genome in early embryonic development in mouse, but not in human. PRJCA016057, GSA for Human Genome Sequence Archive. 2025. https://bigd.big.ac.cn/gsahuman/browse/HRA004381 . Cited 2025 Apr 25.
65. Hou C, Tian GG, Hu S, et al. RNA polymerase I is essential for driving the formation of 3D genome in early embryonic development in mouse, but not in human. CRA010655, GSA Genome Sequence Archive. 2025. https://ngdc.cncb.ac.cn/gsa/browse/CRA010655 . Cited 2025 Apr 25.
66. Hou C, Tian GG, Hu S, et al. RNA polymerase I is essential for driving the formation of 3D genome in early embryonic development in mouse, but not in human. PRJNA989148, NCBI Sequence Read Archive. 2025. https://www.ncbi.nlm.nih.gov/geo/query/acc.cgi?acc=GSE236161 .Cited 2025 Apr 25.

Publisher's Note